Tourmaline Breccias from the Río Blanco-Los Bronces Porphyry Copper District, Chile: Constraints on the Fluid Source and the Utility of Tourmaline Composition for Exploration

Michael Hohf,[1] Robert B. Trumbull,[2,†] Patricio Cuadra,[3,*] and Marco Solé[3]

[1]*Geological Institute, Technische Universität Bergakademie Freiberg, Freiberg 09599, Germany*

[2]*German Research Centre for Geosciences GFZ, Telegrafenberg, Potsdam 14473, Germany*

[3]*División Andina, CODELCO-Chile, Sta. Teresa 513, Los Andes, Chile*

Abstract

Tourmaline-cemented breccia bodies host much of the ore in the Río Blanco-Los Bronces porphyry Cu-Mo deposits. We determined the chemical and B isotope composition of tourmaline as well as S isotope ratios of anhydrite and sulfide minerals to shed light on the composition and origin of mineralizing fluids. Also, the utility of tourmaline as an indicator mineral was tested by comparing mineralized and barren breccias. Tourmaline in mineralized samples has a narrow Mg range (1.5–2 apfu) and variable, generally low Al contents (4–6.5 apfu). A strong negative correlation of Al with Fe indicates monovalent substitution of Al and Fe^{3+}, implying relatively oxidizing fluids. In contrast, tourmaline from barren breccias has a narrower Al range (6–7 apfu), lower and more variable Mg (0.2–2.5 apfu), and a strong negative Mg-Fe correlation, suggesting more reduced fluids with a dominance of Fe^{2+}. These features and the implications of redox contrast may have exploration significance. Tourmaline from all breccia samples yielded $\delta^{11}B$ values from 1.8 to 7.9‰. A magmatic source of boron is concluded from the identical B isotope values of granite-hosted tourmaline in the district (1.2–7.7‰) and from the similar range of regional volcanic and porphyry rocks in the Central Andes. The $\delta^{34}S$ values of coexisting anhydrite (11.6–14.5‰) and chalcopyrite (–1.5 to –0.2‰) in mineralized breccia give S isotope exchange temperatures of 377° to 437°C, consistent with fluid inclusion temperatures. Total sulfur $\delta^{34}S_{fluid}$ estimates between 1.4 ± 3.9 and 8.8 ± 1.3‰ are broadly consistent with a magmatic source but not well constrained. However, published O and H isotope ratios of quartz and tourmaline from the Río Blanco-Los Bronces breccias have a clear magmatic signature, so this is the preferred scenario. Mass balance simulations of the boron budget show that typical magma flux rates, water contents, and boron concentration for the Central Andes could produce the estimated 10^7 tons of boron in the Río Blanco-Los Bronces breccias within the 4-m.y. duration of porphyry intrusions if (1) magma accumulated and evolved at midcrustal levels before emplacement and (2) boron partitioned strongly to the fluid phase ($D^B_{fluid/melt} > 3$).

Introduction

The supergiant Río Blanco-Los Bronces porphyry copper district in the high Andes of central Chile contains one of the largest global resources of copper (200 Mt of Cu metal; Toro et al., 2012). The deposits in the Río Blanco-Los Bronces district are distinctive because of the abundance of tourmaline-cemented breccia bodies, which constitute a large proportion of the copper ore. The tourmaline breccias in the district have been well studied from a geologic, lithologic, and structural context (e.g., Warnaars et al., 1985; Vargas et al., 1999; Piquer et al., 2015). Investigations of fluid inclusions and stable O, H, and S isotope variations have been made (e.g., Kusakabe et al., 1984; Skewes et al., 2003; Frikken et al., 2005), but surprisingly little attention has been paid to the composition of tourmaline (12 analyses in Skewes et al., 2003). An exception is the unpublished work of Testa (2019), who reported a large number of major and trace element analyses of tourmaline from the Río Blanco-Los Bronces district, including 14 B isotope analyses.

The study reported here focuses on the chemical and B isotope composition of tourmaline from two breccia bodies

carrying economic Cu mineralization (La Americana and Sur-Sur) and one occurrence of unmineralized breccia and associated granite-hosted tourmaline nodules from the Diamante prospect, located a few km northwest of the mineralized area. This paper compares the chemical and boron isotope composition of tourmaline from barren and mineralized breccia bodies and discusses the potential of tourmaline composition as a guide to economic mineralization. Although the emphasis is on the tourmaline, we also determined S isotope ratios of chalcopyrite, pyrite, and anhydrite from the mineralized breccias and from previously unstudied late-stage enargite-bearing veins. The boron and sulfur isotope results are combined with existing O, H, and S isotope data for constraining the source of mineralizing fluids and the origin of the huge boron concentration represented by the Río Blanco-Los Bronces breccias.

Regional Setting

The Río Blanco-Los Bronces district is situated in the Mio-cene-Pliocene volcanic arc (western Cordillera) of the southern Central Andes at about 33.15°S longitude, 70.25°W latitude, and 3,500 to 4,000 meters above sea level. The district is located in the Central Chilean copper belt described by Sillitoe and Perelló (2005) along with two other supergiant

---

porphyry copper deposits: Los Pelambres-El Pachón and El Teniente (Fig. 1). In a geodynamic context, the Central Chilean belt is within the "flat-slab" region of the Andes, which is characterized by a shallow dip of the subduction zone and a lack of post-Pliocene volcanism, both features being attributed to subduction of the Juan Fernández Ridge (e.g., Kay and Mpodozis, 2001; Yañez et al., 2001). Kay et al. (1999) and Sillitoe and Perelló (2005) reviewed possible relationships between copper mineralization and geodynamic factors for the Central Andean copper province as a whole (e.g., crustal thickening and uplift, ridge subduction, subduction erosion and arc migration, trans-arc lineaments), while Skewes and Stern (1995) discussed how these factors may relate to the genesis of the Río Blanco-Los Bronces and other supergiant copper deposits in the Central Chilean belt.

Geology of the Río Blanco-Los Bronces District

The Río Blanco-Los Bronces deposits, and those of the El Teniente and Los Pelambres-El Pachón nearby, are hosted in volcanic and volcanic-sedimentary units of the Oligocene-Miocene Abanico basin (Fig. 1). These units are grouped into a lower Abanico Formation and an upper Farellones Formation. According to Piquer et al. (2015) and references therein, the Abanico Formation (34–22 Ma) was deposited in an extensional intra-arc basin, whereas the Farellones Formation volcanic and volcaniclastic rocks (ca. 22–17 Ma) were deposited in a compressional regime of basin inversion that caused folding of the Abanico rocks and reactivated basin-margin structures as reverse faults. Underlying this Cenozoic volcanic-sedimentary sequence is a Jurassic to Cretaceous sedimentary section which, importantly, hosts marine limestones and evaporite beds (Piquer et al., 2015). Figure 2 shows a simplified geologic map of the Río Blanco-Los Bronces district with location of the areas sampled for this study. In this paper, the term "mine area" indicates the main area of mining in the district (Los Bronces, Río Blanco, Sur-Sur, Don Luis, and La Americana localities). A second focus of this study is on nonmineralized tourmaline breccias in the Diamante exploration project to the northwest of the mine area (Fig. 2). Intrusive rocks in the Río Blanco-Los Bronces district are dominated by the San Francisco batholith, which has outcrop dimensions of about 30 km N-W and 20 km E-W. An extensive compilation of U-Pb zircon ages by Toro et al. (2012), together with a few more recent studies, shows that the batholith comprises several units that were assembled over the time span from about 16 to 8 Ma, and that there is a spatial age progression from northwest to southeast. The oldest unit (16.4 ± 0.2 Ma; Piquer et al., 2015) is syenogranite in the northwestern part of the district, including the Diamante area studied here (Fig. 2), while dioritic and granodiorite intrusions in the mine area (Río Blanco and Don Luis) yielded ages from 8.8 ± 0.05 to 8.4 ± 0.2 Ma (Toro et al., 2012). Crosscutting the batholith are a number of andesitic to dacitic porphyry intrusions (stocks and dikes) and breccia bodies located along a broad NW-SE–oriented zone, which Toro et al. (2012) refer to as the Río Blanco-Los Bronces-Los Sulfatos structural corridor (Fig. 2). The total duration of porphyry intrusions in this zone ranged from about 13 to 5 Ma based on zircon U-Pb ages in Toro et al. (2012) and Deckart et al. (2005, 2013, 2014). However, the greatest abundance of
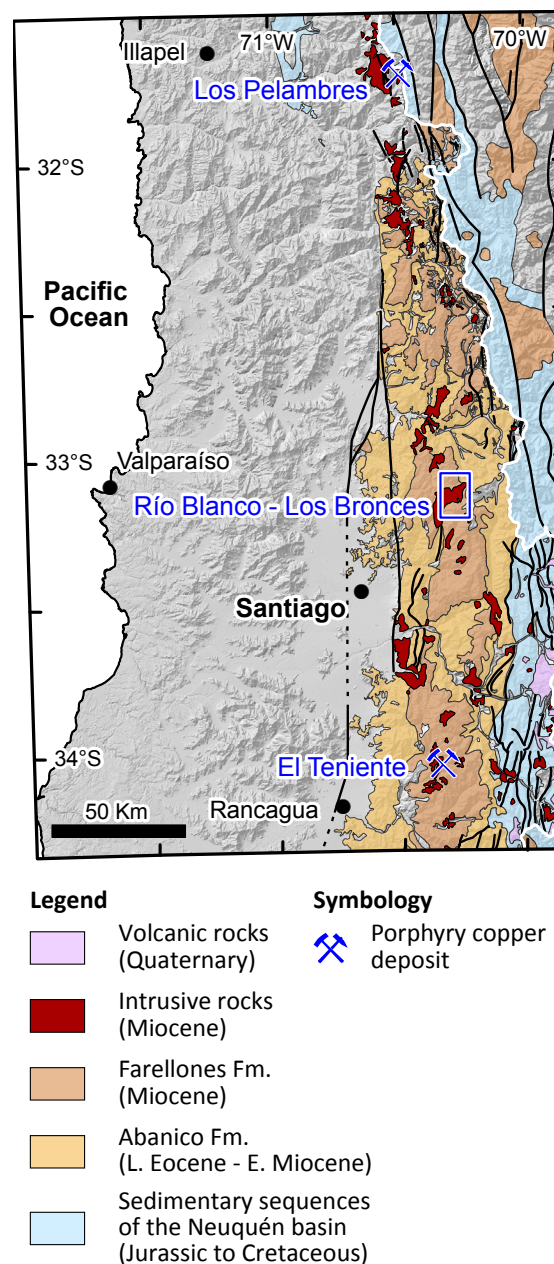

Fig. 1. Location map and simplified geology of the Río Blanco-Los Bronces, El Teniente, and Los Pelambres porphyry copper deposits; elevation data from U.S. Geological Survey EROS center, geology after SERNAGEOMIN (2002). White line is the national border; blue box is location of Figure 2.

porphyry intrusions and concentration of ages is in the mine area, where U-Pb dating shows a continuous span of activity from 8.2 ± 0.5 to 5.0 ± 0.1 Ma. The end of igneous activity in the Río Blanco-Los Bronces district is marked by the La Copa volcanic complex in the northern part of the mine area (Fig. 2), which yielded zircon U-Pb ages from 4.92 ± 0.09 to 4.31 ± 0.05 Ma (Toro et al., 2012).

The copper mineralization in the mine area is closely associated in time and space with dacitic porphyry intrusions. The orebodies comprise stockwork quartz-sulfide veins and disseminated sulfide mineralization in altered porphyries and
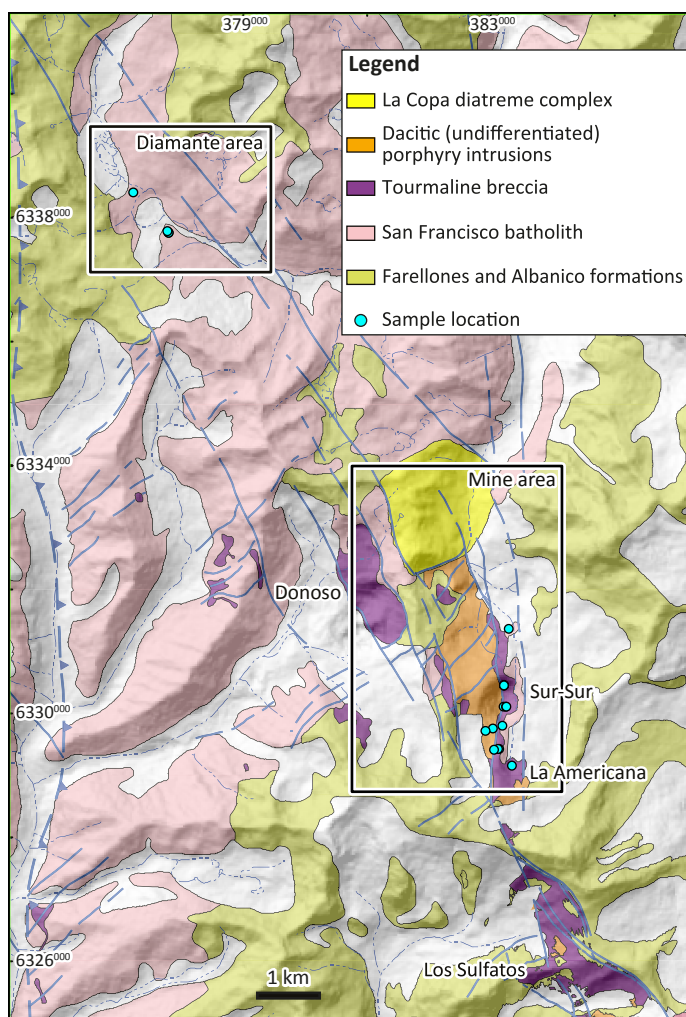
Fig. 2. Simplified geologic map of the Río Blanco-Los Bronces district after Toro et al. (2012); elevation data from U.S. Geological Survey EROS center. Sample locations are shown in the mine area (Sur-Sur and La Americana sectors) and in the Diamante prospect to the northwest.

breccia bodies. Toro et al. (2012) provided an overview of the timing of intrusion, alteration, and mineralization events, while descriptions of the breccia-hosted deposits are given by Vargas et al. (1999) for Donoso, Sur-Sur, and La Americana, by Skewes et al. (2003) for Donoso, by Frikken et al. (2005) for Sur-Sur and by Irarrázaval et al. (2010) for Los Sulfatos. Supergene ores and alteration zones are virtually absent in the district due to erosion. The hypogene Cu-Mo mineralization is dominated by chalcopyrite and bornite with minor molybdenite. The timing of mineralization in the mine area is well constrained by Re-Os dating of molybdenite at about 7 to 5 Ma. Specifically, these ages are 6.07 ± 0.03 and 5.9 ± 1.1 Ma for Río Blanco, 5.6 ± 2.2 and 5.52 ± 0.03 Ma for Sur-Sur, 5.65 ± 0.03 and 5.35 ± 0.03 Ma for Los Bronces, 5.61 ± 0.03 Ma for La Americana), and 7.44 ± 0.03 and 6.40 ± 0.06 Ma for Los Sulfatos (Toro et al., 2012).

The timing of breccia formation is constrained from $^{40}Ar/^{39}Ar$ dating of K-feldspar, sericite, and biotite in breccia matrix (Toro et al., 2012; Deckart et al., 2013) and by crosscutting relationships with dated porphyry intrusions. The $^{40}Ar/^{39}Ar$ dates

from the mine area are in the same 7 to 5 Ma range as the Re-Os mineralization ages; namely: 7.3 ± 0.1 Ma for Los Sulfatos, 6.13 ± 1.1 to 4.78 ± 0.04 Ma for Sur-Sur, 4.65 ± 0.1 Ma for Don Luis, and 5.31 ± 0.17 to 4.36 ± 0.16 Ma for Río Blanco. These ages are minima because the dated minerals formed in breccia matrix and at clast margins after brecciation took place. The maximum age for tourmaline breccia in the Don Luis area is 5.8 Ma because it crosscuts a dacitic porphyry dated at 5.84 ± 0.05 Ma by U-Pb zircon. Similarly, tourmaline breccia in the Río Blanco area cuts a dacitic porphyry dated at 6.0 ± 1.3 Ma and must be younger than that unit.

Hydrothermal alteration and fluid inclusion characteristics have been described by Vargas et al. (1999), Skewes et al. (2003), and Frikken et al. (2005). Hydrothermal alteration is manifested by halos around mineralized veins in porphyry host rocks and by alteration of rock clasts and matrix in the breccia bodies. All authors describe a vertical zonation whereby the deeper levels display potassic alteration dominated by secondary biotite and K-feldspar ± magnetite ± sulfides, which grades upward and outward to a phyllic zone with quartz, sericite, and tourmaline ± chlorite ± magnetite ± hematite ± sulfides ± anhydrite. Weak propylitic alteration (chlorite, epidote, hematite, tourmaline) in the distal parts of the Los Bronces (Donoso) breccia was described by Warnaars et al. (1995). Fluid inclusion studies (Vargas et al., 1999; Skewes et al., 2003; Frikken et al., 2005) revealed three types of inclusions in breccia-matrix quartz and tourmaline: (1) three-phase inclusions (vapor, liquid, salt) and two-phase variants—(2) vapor dominant or (3) liquid dominant. All studies concur that multiple fluid types circulated at different times in the breccia matrix, presumably reflecting changes from hydrostatic to lithostatic pressure conditions and multiple intrusive episodes. There is a correspondingly wide range of temperature and salinity estimates recorded. Homogenization temperatures typically range between 250° and 500°C but were locally higher (550° to >600°C); salinities vary from moderate to hypersaline (a few wt % NaCl up to approx. 50 wt % NaCl equiv). According to Skewes et al. (2003), inclusions that homogenize by halite dissolution (276° to 468°C) trapped high-temperature/high-salinity, single-phase fluid, which probably represent magmatic fluids released under relatively high (lithostatic) pressure conditions. High-temperature saline inclusions that homogenize to the liquid phase locally coexist with vapor-rich inclusions, suggesting boiling conditions during trapping and lower (hydrostatic) pressure.

The tourmaline breccias

Hydrothermal breccia complexes are a first-order feature of the Río Blanco-Los Bronces district with major economic significance, so they have been mapped and studied in detail. Papers by Warnaars et al. (1985), Vargas et al. (1999), Skewes et al. (2003), and Frikken et al. (2005) give detailed descriptions from which this summary is derived. The study of Frikken et al. (2005) is particularly relevant because it describes the Sur-Sur breccia body from which many of our samples were taken. There are several varieties of breccia in the Río Blanco-Los Bronces district, and a complex nomenclature has resulted that combines terms based on locality, texture, clast lithology, and the mineralogy of breccia matrix. There is a strong structural control on the distribution of breccia bodies and their associ-

ated porphyry stocks and dikes. All are distributed for about 6 km along a fault zone extending from the Los Sulfatos deposit in the southeast to the Diamante prospect in the northwest (Fig. 2). Skewes et al. (2003) mentioned 15 breccia bodies in the district that range in diameter from tens of meters to 800 meters, typically have steep to vertical contacts and a vertical extent of at least one kilometer, but their roots are not exposed. Generally speaking, the breccias consist of monolithic clasts of the local wall rock (granitoids of the San Francisco Batholith, andesite of the Farellones, and/or Abanico Formation or one of the porphyry stocks) in a matrix that has been partly or wholly replaced by hydrothermal tourmaline, biotite, actinolite, K-feldspar, quartz, anhydrite, sulfide minerals, and Fe oxides. The rounding of fragments and the relative proportion of matrix to clasts increases from the margins to the center of the breccia body, grading from intensely fractured host intrusion with incipient stockwork veining, through "crackle breccia" zones to a breccia containing up to ~30 vol % matrix and local, highly comminuted "rock flour." The clasts commonly display an alteration zonation with albite–K-feldspar on the edges and greenish biotite in the center.

As described above, previous workers established a vertical zonation of the breccia matrix mineralogy, with fine-grained biotite and K-feldspar dominant in deeper levels (potassic alteration zone) and tourmaline ± sericite in shallower levels (phyllic alteration zone). A vertical zonation in the iron oxide minerals has also been reported (Vargas et al. 1999), with magnetite in deeper zones grading upward to hematite (specularite) in shallower levels. Anhydrite is an important mineral in the breccia matrix, which is locally abundant enough to inspire the name, anhydrite breccia. Surface and near-surface exposures of breccia may show rock-flour matrix with rounded and rotated clasts and/or pebble dikes that reflect a stronger comminution of clasts (Skewes et al., 2003). Mineralization within the breccias comprises disseminated sulfide minerals (chalcopyrite-pyrite-bornite ± molybdenite) in the matrix as well as in altered clasts, and also in crosscutting veinlets (e.g., Fig. 3b). The cited studies remarked on the complex, multistage development of brecciation and mineralization as shown by clasts of one breccia type included in another, by mineralization in rock clasts that does not continue into the matrix, or by quartz-sulfide veinlets that crosscut the breccia matrix and clasts.

Tourmaline is commonly described as an early-formed mineral in the breccia matrix (Vargas et al, 1999; Frikken et al., 2005), but there are multiple growth episodes of tourmaline and other hydrothermal minerals that are related, according to Vargas et al. (1999), to repeated phases of brecciation and hydrothermal cementation of the matrix. The paragenetic sequence of Frikken et al. (2005) for the Sur-Sur breccia starts with an early oxide stage of breccia fill that includes major amounts of tourmaline with biotite and anhydrite, followed by the mineralization stage where sulfide minerals, magnetite and/or hematite, and quartz are the main minerals. According to these authors, tourmaline reenters the paragenetic sequence later in the mineralization stage. Tourmaline also occurs locally in crosscutting quartz-sericite-sulfide veins, which also contain anhydrite and hematite (Warnaars et al., 1985; Vargas et al., 1999; Skewes et al., 2003). Finally, Warnaars et al. (1985) described prebreccia tourmalinization in the form

of nodules or veins in the granitic host rock, which are associated with sulfide-poor, barren tourmaline breccias. This paper presents tourmaline data from a similar occurrence of barren tourmaline breccias and tourmaline nodules in the associated granite at the Diamante prospect.

Sample Descriptions

This investigation covers 14 samples from mineralized breccia in two sectors of the mine area (Sur-Sur: 7 samples; La Americana: 7 samples), selected to represent a range of breccia types and degrees of mineralization based on their Cu assay values (Table 1). The mine area samples come from drill cores. An additional four samples were taken from outcrops in the Diamante prospect to the northwest of the mine area, where barren tourmaline breccia and tourmaline-quartz nodules in the granitic host rock are exposed. Two samples of the barren breccia were collected as well as two samples of quartz-tourmaline in the host granite to represent the composition of magmatic tourmaline. Electron microprobe analyses were made on all samples. Secondary ion mass spectrometry (SIMS) isotope analyses were performed on six mineralized breccia samples and on all four samples from Diamante. The selection of samples for sulfur isotope analyses (bulk mineral separates) was divided between mineralized breccias and late-stage enargite-bearing veins (see Table 1). For more sample details including coordinates see the data publication by Hohf and Trumbull (2022).

Mine area: La Americana and Sur-Sur

Six varieties of breccia, according to the nomenclature of the mine (see Vargas et al., 1999), are represented in our samples (Table 1). The most common is the tourmaline breccia (BXT), which is represented here by three samples from Sur-Sur and one from La Americana. The BXT breccia is a clast-supported crackle breccia containing angular, monolithic clasts of the respective host rocks (San Francisco granitoids, andesite and dacite porphyries). The clasts show little or no relative displacement or rotation from one another (Fig. 3a), and they are strongly affected by quartz-sericite ± tourmaline ± pyrite alteration. The matrix (5–20 vol %) is made up mainly of tourmaline and quartz, with minor magnetite and/or pyrite, biotite, albite, and rock flour. A second variety of tourmaline-cemented breccia, called BXTTO ("tuffaceous" due to abundant rock flour in the matrix), is polymict and contains subangular to subrounded clasts of volcanic rocks, granodiorite, dacitic porphyry and, importantly, clasts of the BXT breccia. The matrix of BXTTO contains tourmaline and chlorite along with varying amounts of quartz, K-feldspar, plagioclase, pyrite, and lesser biotite. Frikken et al. (2005) described the BXTTO breccia at Sur-Sur as postmineralization, but our BXTTO samples yielded assay values of around 1 wt % Cu (Table 1). Two other breccia varieties in the sample set are of minor importance. They resemble the BXT breccia but are distinguished by a relatively high abundance of other matrix phases, either biotite (mine code BXB), anhydrite (mine code BXANH) or specularite (mine code BXSPEC). The breccia type BXMN is a variety of rock flour breccia with biotite and chlorite but no tourmaline in the matrix. We included two samples of BXMN in this study for analysis of chalcopyrite sulfur isotope composition.
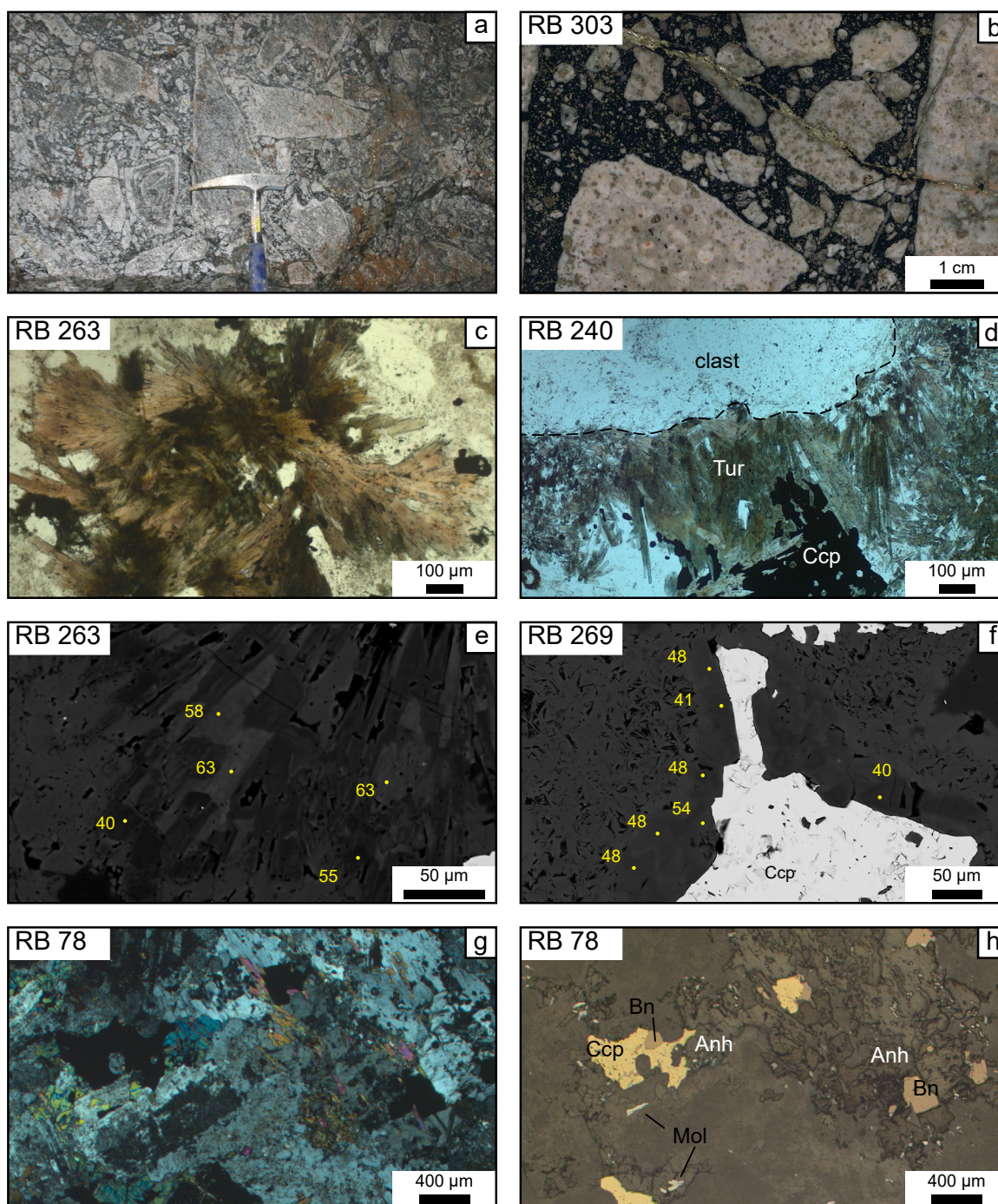
Fig. 3. Outcrop- and sample-scale images of mineralized tourmaline breccia in the mine area. (a) Underground exposure of the tourmaline breccia (BXT), Sur-Sur; (b) hand specimen of BTX breccia, sample RB303, La Americana, showing mineralized breccia cut by a quartz-sulfide veinlet; (c) radial tourmaline in breccia matrix, sample RB263, Sur-Sur, plane-polarized light (PPL); (d) acicular tourmaline intergrown with chalcopyrite (Ccp) around a porphyry clast in breccia, sample RB240, Sur-Sur, PPL; (e) backscattered electron image of acicular tourmaline from sample RB263, Sur-Sur, showing patchy zoning and microprobe points with corresponding Fe# [Fe/(Fe+Mg)*100] in yellow; (f) backscattered electron image of "felty" tourmaline aggregate intergrown with chalcopyrite (Ccp) from sample RB269, Sur-Sur, with microprobe points and corresponding Fe# [Fe/(Fe+Mg)*100] in yellow; (g,h) photomicrographs in cross-polarized light and reflected light, respectively, of anhydrite (Anh) intergrown with bornite (Bn) and chalcopyrite (Ccp) in sample RB78, La Americana.

Tourmaline in the breccia matrix of La Americana and Sur-Sur samples is black in hand specimen (Fig. 3b) and brown to olive colored in thin section (Fig. 3c, d). Tourmaline grains commonly form radial aggregates (Fig. 3c), short, acicular crystals on the margins of rock clasts, or dense, felted masses in the matrix associated with sulfide minerals and quartz (Fig. 3d). Optical zoning is common and diverse, even in single thin sections, with examples of irregular, patchy zoning and

Table 1. List of Samples Investigated

Sample	Area	Drill hole/depth (m)	Lithology[1]	Alteration	Ore minerals	Cu (wt %)	Elevation (m)
[S]RB8	LA	4217/745	BXTTO	Potassic	Py/Ccp	1.5	3,519
[B,S]RB11	LA	4217/818	BXTTO	Potassic	Ccp>Py	1.6	3,452
RB13	LA	4217/1067	BXANH	Propylitic	Ccp>Py	1.3	3,212
RB22	LA	4377/169	BXSPEC	Propylitic	Py/Ccp	0.16	4,166
[S]RB78	LA	4663/502	BXMN	Potassic	Ccp>Bn	3.4	3,165
[S]RB101	LA	4663/310	BXMN	Potassic	Ccp>Py	1.2	2,978
[S]RB112	LA	4663/503	BXANH & vein	Anh/gypsum	Cct/Bn	15.9	2,832
[B,S]RB231	SS	TSS-22/297	BXT	Qz-sericite	Py/Ccp	1.0	3,362
RB240	SS	TSS-22/424	BXB	Potassic	Ccp>Py	0.87	3,236
[S]RB244	SS	TSS-22/483	BXT	Potassic	Ccp>Py	0.54	3,177
[B,S]RB263	SS	TSS-33/118-120	BXTTO	Potassic	Ccp>Py	0.93	3,778
[B,S]RB269	SS	TSS-33/233-251	BXT	Potassic	Ccp>Py	3.5	3,894
RB271	SS	TSS-33/251	BXT	Potassic	Ccp>Py	7.2	3,902
[S]RB299	DL	Outcrop	Vein	Gypsum	Cct-Apy	n.a.	3,574
[B]RB304	DI	Outcrop	Nodule	None	Barren	n.a.	3,385
[B]RB305	DI	Outcrop	BXT	Sodic	Barren	n.a.	3,385
[B]RB306	DI	Outcrop	Nodule in BXT	Sodic	Barren	n.a.	3,405
[B]RB322	DI	Outcrop	BXT	Potassic	Barren	n.a.	3,379

Notes: Samples RB78, RB101, RB112, RB244 and RB299 do not contain tourmaline; superscript B and S denote samples analysed for B and S isotopes, respectively; Cu wt % values are for whole-rock samples

Abbreviations: DI = Diamante, DL = Don Luis, LA = La Americana, n.a. = not analyzed, SS = Sur-Sur

Mineral abbreviations: Apy = arsenopyrite, Bn = bornite, Ccp = chalcopyrite, Cct = chalcocite, Py = pyrite

[1]Lithology codes: BXANH = anhydrite breccia, BXB = biotite breccia, nodule= tourmaline-quartz segregation in granite (RB304) or granite clast in BXT (RB306), BXMN = "monolito" rock flour breccia, biotite-chlorite breccia, BXSPEC = specularite breccia, BXT = tourmaline breccia, BXTTO (Paloma breccia of Vargas et al., 1999) = tuffaceous tourmaline-cemented breccia

concentric growth zoning (examples are shown in the data publication of Hohf and Trumbull [2022]). There are also many cases of unzoned tourmaline. In most samples, tourmaline appears fresh and unaltered under the microscope, but an exception is in the anhydrite breccia sample RB13, where anhedral, embayed grains are partially replaced by biotite and Ti magnetite or rutile.

Diamante area

The Diamante area is a brownfield exploration prospect situated at the northwest extension of the Río Blanco-Los Bronces mineralization corridor, which contains about 30 small tourmaline-quartz-feldspar breccia bodies (up to approx. 200 m²). The main host rock is syenogranite of the San Francisco Batholith (zircon U-Pb age 16.52 ± 0.07 Ma; Hohf, 2021), which contains locally abundant tourmaline-rich nodules in addition to the breccias (Fig. 4a and d, respectively). The tourmaline breccia is a monolithic, clast-supported crackle breccia, locally with a rock flour component, similar to the BXT unit of the mine area but lacking significant sulfide mineralization. The clasts are subangular, with sizes from 0.5 to 30 cm, and show albite-sericite reaction halos against the matrix. The hydrothermal matrix consists of fine- to medium-grained acicular aggregate of prismatic tourmaline (Fig. 4e). Minor minerals in the matrix include quartz, sericitized feldspar, and accessory pyrite. Breccia cavities are partially filled with quartz and coarse-grained (up to 3-cm-long) tourmaline crystals with a radial habit; some cavities also contain rutile and rare monazite.

Two samples of granite-hosted quartz-tourmaline nodules in the Diamante area were studied, and these contain a complex tourmaline paragenesis. Sample RB304 contains irregular-shaped tourmaline-quartz nodules of one- to two-centimeter diameter in which the tourmaline forms aggregates of anhedral grains a few millimeters in size with a uniform

light to dark brown pleochroism. Sample RB306 represents a granite clast in breccia containing irregular, centimeter-sized tourmaline-rich nodules. This sample contains two types of tourmaline. Type 1 resembles that in sample RB304, i.e., anhedral, unzoned grains several millimeters in size with light to dark brown pleochroism. The second, Type 2 tourmaline forms euhedral to subhedral grains, typically less than 1 millimeter in diameter, which have darker brown-green pleochroic colors and strong, concentric color zoning. These euhedral, zoned tourmaline grains form clusters that commonly surround grains of Type 1 tourmaline (Fig. 4b), suggesting that they formed later. In terms of chemical composition, the two textural types of tourmaline overlap.

Analytical Methods

Electron probe microanalyses (EPMA)

All but two samples in this study (RB304 and RB306) were analyzed in the electron microprobe laboratory in Freiberg at the Technische Universität Bergakademie (TUBAF). The others were analyzed in Potsdam at the German Research Centre for Geosciences (GFZ). The microprobe conditions are described separately below. For calculating mineral formulae, all analyses were treated the same way, by normalizing to 15 cations on the Y, Z, or T sites as suggested for Li-poor tourmaline by Henry et al. (2011) and implemented in the software WinTcalc (Yavuz et al., 2014). A selection of typical analyses is shown in Table 2, and the full set with about 460 analyses is reported in the data publication (Hohf and Trumbull, 2022).

The analyses at the TUBAF in Freiberg employed a JEOL JXA-8900R electron microprobe with five wavelength-dispersive spectrometers. The spot analyses were conducted at 20 kV accelerating voltage and a beam current of 12 nA, with a
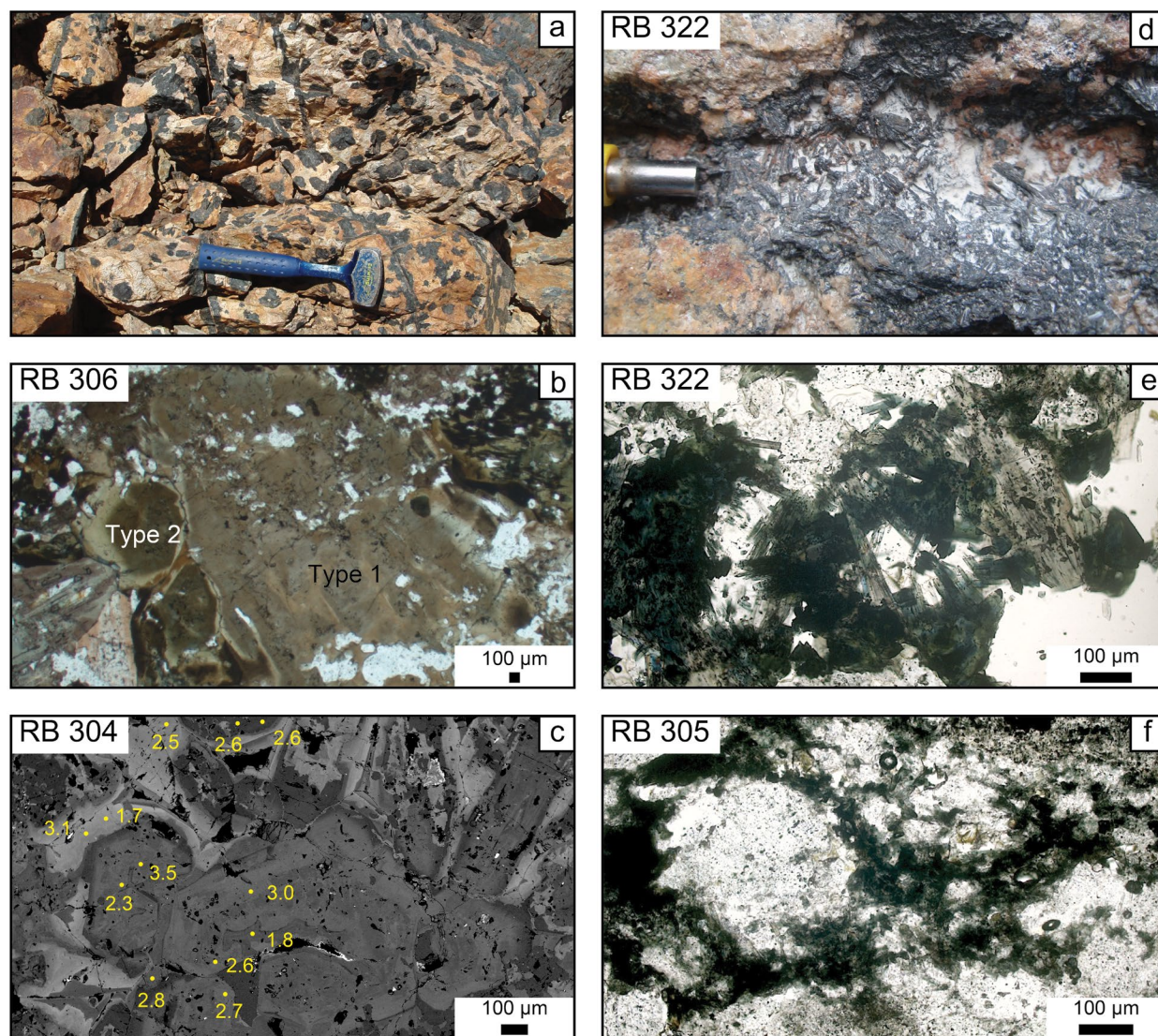
Fig. 4. Outcrop- and sample-scale images of granite-hosted tourmaline nodules and barren tourmaline breccia in the Diamante area. (a) Outcrop of tourmaline nodules in syenogranite; (b) photomicrograph of sample RB306, plane-polarized light, with zoned, subhedral tourmaline (Type 2) overgrowth on large, anhedral Type 1 tourmaline; (c) backscattered electron image of sample RB304 showing a cluster of subhedral, zoned tourmaline Type 2, with secondary ion mass spectrometry (SIMS) $\delta^{11}B$ values (‰); (d) outcrop photo of tourmaline breccia in synenogranite sample RB322; (e, f) photomicrographs in plane-polarized light of tourmaline breccia matrix in samples RB322 and RB305, respectively.

focused beam of 5-µm diameter. The counting times were 15 s on peak for Na; 20 s for Al and Si; 30 s for Fe and Mg; 60 s for Cu, Ti, K, V, Ca, Mn and Cr; and 90 s for F. Background counting times were half of those on the respective peak. Mineral and element standards used for calibration were wollastonite (Ca, Si), diopside (Mg), hematite (Fe), albite (Na), rutile (Ti), orthoclase (K, Al), fluorite (F), rhodonite (Mn), cuprite (Cu), and V-metal (V).

The EPMA analyses at the GFZ Potsdam were carried out with a JEOL JXA 8230 electron microprobe equipped with an LaB$_6$-cathode and five wavelength-dispersive spectrometers. The applied accelerating voltage was 15 kV, beam current was 10 nA, and the beam was focused to a spot diameter of 5 µm. Counting times on peak (twice those on backgrounds) were 10 s for Si, K, and Na; 20 s for Al, F, Ti, Ca, Cl, Mg, Fe, and

Mn; and 30 s for Ba. The following mineral standards were used for calibration: orthoclase (Si, Al, K), rutile (Ti), diopside (Ca, Mg), tugtupite (Cl), synthetic BaSi$_2$O$_5$ (Ba), albite (Na), hematite (Fe), and rhodonite (Mn).

Boron isotope analyses

Boron isotope analyses were conducted with the Cameca 1280-HR SIMS instrument at the GFZ Potsdam on one-inch diameter, round polished thin sections that were cleaned in an ultrasonic bath of pure ethanol, then gold-coated in vacuum with a 35-nm layer thickness. For samples RB304 and RB306, the same round sections were used for SIMS and EPMA analyses, while for all other samples, new round sections were prepared from the rectangular billets used for the EPMA sections analyzed in Freiberg. The analyses employed

a 5-nA, $^{16}O^-$ primary beam with 13 keV energy and a beam diameter of about 5 µm. Secondary ions were extracted with a 10-kV potential and no offset voltage. Analyses were made in multicollection mode with Faraday cups. Each analysis consisted of 20 cycles with integration times of 4 s on ^{10}B and 2 s on ^{11}B per cycle, preceded by a 90-s sputter to remove the gold coating and surface contamination. The mass resolution $M/\Delta M$ was 2,000, more than enough to separate ^{11}B and $^{10}B^1H$ masses. Instrumental mass fractionation and analytical quality were monitored by multiple analyses of reference materials Harvard dravite (#108796) and schorl (#112566), described by Dyar et al. (2001) and Wiedenbeck et al. (2021). The internal precision of single analyses was typically less than 0.1‰ (1 standard deviation/mean of 20 cycles). Repeatability on individual reference materials was between 0.1 and 0.2‰ (1 s.d.). The combined 1 s.d. variability of all analyses from both reference materials was <0.8‰ for each analytical session, which includes any chemical matrix effect and is an estimate for the overall analytical uncertainty. After correction for instrument mass fractionation, the $^{11}B/^{10}B$ ratios were converted to $\delta^{11}B$ values relative to NIST SRM 951 (4.04362) from Catanzaro et al. (1970). The results from all analyses of reference materials and 96 analyses of the Río Blanco-Los Bronces tourmalines are reported in the data publication (Hohf and Trumbull, 2022).

Sulfur isotope analyses

Sulfur isotope analyses were performed on hand-picked mineral separates of anhydrite and sulfide minerals using the ThermoQuest-Finnigan IRMS Delta Plus instrument at the Institute of Mineralogy, TUBAF, Freiberg. For anhydrite, the sample preparation involved dissolution of 100 mg of ground sample in 200 mL of deionized water at room temperature, followed by filtration in a 0.45-µm filter. The filtrate was acidified with 1 mL of 1M HCl and sulfate was precipitated as $BaSO_4$ by adding 1 to 2 mL saturated $BaCl_2$ solution. The $BaSO_4$ was collected on a cellulose acetate/nitrate filter, washed until chloride-free ($AgNO_3$ test) and dried at 40°C. For the sulfide samples, an appropriate mass of ground sample to yield 38 µg S was added with the same amount of V_2O_5 into an Sn capsule and sealed. The sealed mixture was combusted in a stream of oxygen in a high temperature furnace (elemental analyzer CarloErba at 1,020°C) to quantitatively convert the sulfur to SO_2. The samples were measured with a laboratory SO_2 gas standard, a laboratory silver sulfide standard and international standards IAEA -NBS127, -S2 and -S3: IAEA-NBS127 ($BaSO_4$) = +20.3‰ ± 0.4; IAEA-S2 (Ag_2S) = +22.7‰ ± 0.2; IAEA-S3 (Ag_2S) = –32.3‰ ± 0.2; all values based on per-mil variation from Vienna-Canyon Diablo Troilite (V-CDT). The reproducibility of the analyses was ≤0.3‰ at one standard deviation. The results are given in Table 3.

Results

Chemical composition of tourmaline

In the descriptions below, samples are grouped into those from the mine area (five samples from Sur-Sur, four from La Americana) and the Diamante exploration area (four samples).

Tourmaline from the mine area: All samples from breccia in both the Sur-Sur and La Americana sectors plot in the alkali group in terms of X-site occupancy (Henry et al., 2011)

and show a considerable range of X-site vacancies and Ca contents (Fig. 5a). The compositional ranges from Sur-Sur samples (gray) and La Americana samples (black) overlap in terms of these variables, and there is no systematic difference between them nor among the various breccia subtypes. In the Al-Fe-Mg ternary diagram after Henry and Guidotti (1985), most Sur-Sur and La Americana tourmaline data plot as Al-deficient with respect to the schorl-dravite join at 6.0 atoms per formula unit (apfu) total Al (Fig. 5c). However, the total ranges of Al concentration are wide: from 7.4 to 3.9 apfu for Sur-Sur and from 6.5 to 4.7 apfu for La Americana. The tourmaline compositions on this plot form a well-defined array corresponding to a hypothetical tieline between an end member on the Mg-Al join and the Al-free end-member povondraite $[NaFe^{3+}_3Mg_2Fe^{3+}_4Si_6O_{18}(BO_3)_3(OH)_3O]$. The implication of this trend is an exchange of Al and Fe^{3+}, which is examined in more detail below with reference to Figure 6 and later in the discussion. With few exceptions, tourmaline from breccias in the mine area has moderate to low Ca contents (<0.2 apfu). Titanium contents are in a similar range, from near zero to 0.2 apfu (five outliers up to 0.4 apfu).

On the Al-Fe plot (Fig. 6a), the data for both Sur-Sur and La Americana sectors trend parallel with the $AlFe_{-1}$ vector. The combined linear regression yields $Fe = -0.82 \times Al + 6.29$, with a correlation coefficient –0.76 ($n = 271$). The regression line extrapolates to an iron-free endmember with close to 8 Al apfu, corresponding to magnesiofoitite. The steep slope and strong correlation on this plot suggest that Al-Fe variations are mostly due to the homovalent substitution of Al and Fe^{3+}, but deviation from the ideal slope of –1 indicates that other substitutions are involved. The $MgFe_{-1}$ exchange is unimportant, as shown by the vertical array on Figure 6b and a correlation coefficient of 0.09. Other possibilities are coupled substitutions involving vacancies on the X-site (foitite substitution): $(Al\square)(NaFe^{2+},Mg)_{-1}$; or deprotonation on the W-site: $(AlO)[Fe^{2+},Mg(OH)]_{-1}$. Following Medaris et al. (2003), the foitite substitution can be distinguished by a positive correlation of Al and X-site vacancy and a data array with a slope near 1. This is not the case for the mine area tourmaline (Fig. 6c), which yields a rather poorly defined and shallow sloping regression line ($\square = 0.12 \times Al - 0.59$, correlation coefficient 0.50). A measure of the deprotonation substitution can be visualized on a plot of Al $-\square$ against Fe + Mg + $\square$ (Fig. 6d), which removes the effect of X-site vacancies and causes ideal schorl/dravite and foitite/magnesio-foitite to plot together at Al = 6, (Fe + Mg) = 3 (Medaris et al., 2003). The tourmaline data display a well-defined trend on this diagram with a slope of –0.83 and correlation coefficient of 0.90. The majority of analyses plot to the left of the schorl-foitite composition, indicating a predominance of the $AlFe_{-1}$ exchange, while those plotting to the right of schorl-foitite reflect the deprotonation substitution Al + O^{2-} = (Fe^{2+}, Mg) + OH^-).

Most tourmaline crystals in the breccia matrix from the mine area samples are too small and/or too closely intergrown for clean analyses of crystal cores and rims separately. The few examples where zoning in larger grains could be analyzed showed that tourmaline rims commonly have lower Mg/(Fe + Mg) ratios, higher Ca/(Ca + Na), and less Al than cores.

Diamante area samples: Diamante area samples are divided into two groups according to their occurrence in hydrothermal

Table 2. List of Typical Tourmaline Chemical and Boron Isotope Compositions from Different Settings in the Río Blanco-Los Bronces District

Sample	RB8	RB8	RB11	RB11	RB22	RB22	RB231	RB231	RB231	RB263	RB264	RB263	RB304	RB304	RB306	RB306	RB322	RB322	RB305	RB305
Locality	LA	LA	LA	LA	LA	LA	SS	SS	SS	SS	SS	SS	DI	DI	DI	DI	DI	DI	DI	DI
Lithology	BXTTO	BXTTO	BXTTO	BXTTO	BXSPEC	BXSPEC	BXT	BXT	BXT	BXTTO	BXTTO	BXTTO	Nodule	Nodule	Nodule	Nodule	BXT	BXT	BXT	BXT
Grain - spot	6-2	7-2	3-1	3-3	4-1	4-2	1-1	6-1	6-2	9-1	9-3	10-1	A-7	A-8	C-12	C-20	4-1	4-3	5-1	5-2
Position	Interior	Interior	Core	Rim	Core	Interior	Rim	Rim	Core	Rim	Core	Core	Rim	Core	Rim	Core	Rim	Interior	Rim	Interior
SiO_2	34.3	35.0	34.3	34.5	32.6	33.2	35.9	33.1	33.2	36.5	36.02	35.0	34.7	33.9	34.5	34.1	36.5	36.7	36.5	37.7
TiO_2	0.77	0.42	0.25	0.32	0.72	0.31	0.49	0.63	0.48	0.24	0.26	1.32	0.25	1.37	3.06	0.92	0.47	0.39	0.18	0.11
Al_2O_3	28.5	31.5	22.8	23.3	27.5	29.3	30.3	26.3	25.4	27.6	26.91	20.0	30.1	27.1	26.3	31.9	34.7	34.3	31.2	34.1
$FeO^{[1]}$	11.15	8.95	16.17	16.56	15.44	13.62	9.86	13.70	15.38	12.00	14.23	20.82	11.60	10.57	7.10	8.32	6.28	5.74	5.41	2.72
MnO	0.00	0.00	0.00	0.00	0.05	0.09	0.00	0.00	0.00	0.00	0.00	0.00	0.00	0.00	0.02	0.03	0.00	0.00	0.00	0.00
MgO	6.93	7.02	7.25	6.46	5.12	5.18	6.58	7.14	6.14	7.31	6.11	6.44	5.63	8.07	10.14	6.93	6.20	7.14	9.64	8.67
CaO	0.15	0.42	0.92	0.97	1.03	0.59	0.87	1.94	2.12	0.71	0.35	1.05	0.44	1.65	2.02	0.65	0.34	0.38	0.00	0.16
Na_2O	2.40	2.35	2.55	2.42	2.23	2.26	2.14	1.81	1.68	2.58	2.82	2.50	2.27	1.94	1.88	2.31	1.81	2.02	2.94	2.29
K_2O	0.07	0.02	0.03	0.04	0.02	0.02	0.04	0.04	0.03	0.03	0.04	0.04	0.00	0.00	0.00	0.00	0.00	0.04	0.03	0.02
$H_2O^{[1]}$	3.41	3.47	2.61	2.58	3.43	3.40	3.47	2.6	2.6	3.57	3.55	2.63	3.39	3.47	3.53	3.47	3.35	3.44	3.64	3.49
$B_2O_3^{[1]}$	10.2	10.5	9.9	9.9	10.0	10.1	10.4	10.0	9.9	10.4	10.30	10.0	10.2	10.2	10.3	10.4	10.7	10.8	10.7	10.8
Total	98.1	99.6	96.8	97.2	98.2	98.2	100.0	97.4	96.9	101.0	100.6	99.9	98.6	98.2	98.8	99.0	100.3	100.9	100.2	100.0
Si	5.8	5.8	6.0	6.0	5.7	5.7	6.0	5.7	5.8	6.1	6.1	6.1	5.9	5.8	5.8	5.7	5.9	5.9	5.9	6.1
Ti	0.1	0.1	0.0	0.0	0.1	0.0	0.1	0.1	0.1	0.0	0.0	0.2	0.0	0.2	0.4	0.1	0.1	0.0	0.0	0.0
Al	5.7	6.2	4.7	4.8	5.6	5.9	5.9	5.4	5.3	5.4	5.3	4.1	6.0	5.5	5.2	6.3	6.7	6.5	6.0	6.5
Fe	1.6	1.2	2.4	2.4	2.2	2.0	1.4	2.0	2.3	1.7	2.0	3.0	1.6	1.5	1.0	1.2	0.9	0.8	0.7	0.4
Mn	0.0	0.0	0.0	0.0	0.0	0.0	0.0	0.0	0.0	0.0	0.0	0.0	0.0	0.0	0.0	0.0	0.0	0.0	0.0	0.0
Mg	1.8	1.7	1.9	1.7	1.3	1.3	1.6	1.8	1.6	1.8	1.5	1.7	1.4	2.1	2.6	1.7	1.5	1.7	2.3	2.1
Ca	0.0	0.1	0.2	0.2	0.2	0.1	0.2	0.4	0.4	0.1	0.1	0.2	0.1	0.3	0.4	0.1	0.1	0.1	0.0	0.0
Na	0.8	0.8	0.9	0.8	0.8	0.8	0.7	0.6	0.6	0.8	0.9	0.8	0.7	0.6	0.6	0.7	0.6	0.6	0.9	0.7
K	0.0	0.0	0.0	0.0	0.0	0.0	0.0	0.0	0.0	0.0	0.0	0.0	0.0	0.0	0.0	0.0	0.0	0.0	0.0	0.0
$B^{[1]}$	3.0	3.0	3.0	3.0	3.0	3.0	3.0	3.0	3.0	3.0	3.0	3.0	3.0	3.0	3.0	3.0	3.0	3.0	3.0	3.0
T-site																				
Si(T)	5.8	5.8	6.0	6.0	5.7	5.7	6.0	5.7	5.8	6.1	6.1	6.1	5.9	5.8	5.8	5.7	5.9	5.9	5.9	6.1
Al(T)	0.1	0.2	0.0	0.0	0.3	0.3	0.0	0.2	0.2	0.0	0.0	0.0	0.1	0.2	0.2	0.3	0.1	0.1	0.1	0.0
Z-site																				
Al(Z)	5.6	6.0	4.7	4.8	5.4	5.7	5.9	5.1	5.1	5.4	5.3	4.1	5.9	5.3	5.1	6.0	6.0	6.0	5.9	6.0
Mg(Z)	0.4	0.0	1.3	1.2	0.6	0.3	0.1	0.9	0.9	0.6	0.7	1.7	0.1	0.7	0.9	0.0	0.0	0.0	0.1	0.0
Y-site																				
Al(Y)	0.0	0.0	0.0	0.0	0.0	0.0	0.0	0.0	0.0	0.0	0.0	0.0	0.0	0.0	0.0	0.0	0.6	0.5	0.0	0.5
Ti(Y)	0.1	0.1	0.0	0.0	0.1	0.0	0.1	0.1	0.1	0.0	0.0	0.2	0.0	0.2	0.4	0.1	0.1	0.0	0.0	0.0
Fe(Y)	1.6	1.2	2.4	2.4	2.2	2.0	1.4	2.0	2.3	1.7	2.0	2.8	1.6	1.5	1.0	1.2	0.9	0.8	0.7	0.4
Mn(Y)	0.0	0.0	0.0	0.0	0.0	0.0	0.0	0.0	0.0	0.0	0.0	0.0	0.0	0.0	0.0	0.0	0.0	0.0	0.0	0.0
Mg(Y)	1.3	1.7	0.6	0.5	0.7	1.0	1.6	1.0	0.7	1.2	0.9	0.0	1.3	1.3	1.6	1.7	1.5	1.7	2.3	2.1
X-site																				
Ca(X)	0.0	0.1	0.2	0.2	0.2	0.1	0.2	0.4	0.4	0.1	0.1	0.2	0.1	0.3	0.4	0.1	0.1	0.1	0.0	0.0
Na(X)	0.8	0.8	0.9	0.8	0.8	0.8	0.7	0.6	0.6	0.8	0.9	0.8	0.7	0.6	0.6	0.7	0.6	0.6	0.9	0.7
K(X)	0.0	0.0	0.0	0.0	0.0	0.0	0.0	0.0	0.0	0.0	0.0	0.0	0.0	0.0	0.0	0.0	0.0	0.0	0.0	0.0
Vacancy	0.2	0.2	0.0	0.0	0.1	0.1	0.1	0.0	0.0	0.0	0.0	0.0	0.2	0.1	0.0	0.1	0.4	0.3	0.1	0.3
Mg/(Fe+Mg)	0.53	0.58	0.44	0.41	0.37	0.40	0.54	0.48	0.42	0.52	0.43	0.36	0.46	0.58	0.72	0.60	0.64	0.69	0.76	0.85
$\delta^{11}B$	n.d.	n.d.	4.0	5.6	n.d.	n.d.	3.0	5.3	3.4	4.4	4.8	3.8	6.8	6.1	1.2	3.3	3.2	4.4	7.4	3.0

Localities: DI = Diamante, LA = La Americana, SS = Sur-Sur

Lithologies: BXSPEC = specularite breccia, BXT = tourmaline breccia, Nodule = tourmaline-quartz nodules in granite, BXTTO = tuffaceous tourmaline breccia

[1] calculated with WinTcalc (Yavuz et al., 2014) assuming 3.0 apfu boron, complete OH occupancy of W and Z sites, all Fe as FeO

Table 3. List of Sulfur Isotope Analyses

Sample	Area	Lithology	Mineral	$\delta^{34}S$	$\Delta^{34}S$ (Anh-Ccp)	T°C[1]
RB8	LA	BXTTO	Ccp	–1.5	15.3	389
			Anh	13.8		
RB11	LA	BXTTO	Ccp	–1.5	n.a	n.a
RB78	LA	BXMN	Ccp	–2.4	14.0	420
			Mo	–2.2		
			Anh	11.6		
RB101	LA	BXMN	Ccp	–2.0	n.a	n.a
RB112	LA	Vein	Bn	–2.4	n.a	n.a
			En	–3.9		
			Anh	9.3		
RB231	SS	BXT	Ccp	–1.3	15.8	377
			Anh	14.5		
RB244	SS	BXT	Ccp	–0.3	13.4	437
			Mo	–0.2		
			Anh	13.1		
RB263	SS	BXTTO	Ccp	–1.3	n.a	n.a
RB269	SS	BXT	Ccp	–2.5	n.a	n.a
RB299	DL	Vein	En	0.5	n.a	n.a
			Py	1.0		
			Aln	0.8		

Note: Analyses on mineral separates, uncertainty of $\delta^{34}S \pm 0.3$ ‰ (see methods)

Abbreviations: Aln = alunite, Anh = anhydrite, Bn = bornite, BXMN = rock flour breccia, BXT = tourmaline breccia, BXTTO = tuffaceous tourmaline breccia, Ccp = chalcopyrite, DL = Don Luis, En = enargite, LA = La Americana, Mo = molybdenite, n.a. = not applicable (no mineral pair), Py = pyrite, SS = Sur-Sur

[1] S isotope exchange temperature (Anh-Ccp) based on Ohmoto and Lasaga (1982)

breccia (samples RB305, RB322) or granite-hosted nodules (samples RB304, RB306). The breccia-hosted tourmaline has relatively low Ca contents (up to 0.13 apfu) and a wide range of alkali/vacancy ratios (Fig. 5b). On the Al-Fe-Mg ternary, these tourmalines plot roughly along the dravite-schorl join (Fig. 5d), with Mg/(Mg + Fe) values from 0.1 to 0.9 and total Al contents from 5.9 to 7 apfu. The composition of tourmaline from granite nodules is quite different. The two textural types described above (see Fig. 4b) overlap in composition and are not plotted separately; both are compositionally distinct from the breccia-hosted tourmaline in several ways. First, the granite-hosted tourmaline is comparatively rich in Ca (up to 0.52 apfu) and poor in X-site vacancies (Fig. 5b). Also, the nodule tourmaline is richer in Ti than breccia-hosted tourmaline (maximum 0.45 apfu) and third, most analyses of the nodule tourmaline plot below the schorl-dravite join on Fig. 5d (Al contents are as low as 4.5 apfu).

Other compositional contrasts of the breccia- and granite-hosted tourmaline from Diamante are shown on Figure 6 with reference to possible substitution mechanisms as described above for the mine area. The Al-Fe plot (Fig. 6e) shows a roughly vertical trend for the breccia-hosted tourmaline, with a limited range of Al and poor correlation with Fe (correlation coefficient 0.14). The nodule-hosted tourmaline shows a wide range of both Al and Fe on this plot and a weak negative correlation (Fe = $-0.60 \times$ Al + 4.7, correlation coefficient 0.30). The Mg-Fe plot (Fig. 6f) shows a stronger contrast between the two tourmaline groups. The breccia samples form a well-defined line (regression equation Fe = $-0.68 \times$

Mg + 2.01, correlation coefficient = 0.80) that suggests the $MgFe_{-1}$ substitution and hence a dominance of divalent Fe in these samples (see discussion). The nodule-hosted tourmaline shows only a weak negative correlation on this plot (correlation coefficient 0.39), which indicates the influence of other substitution mechanisms. Coupled substitutions involving Al and X-site vacancies are examined in Figure 6g. The breccia-hosted tourmaline shows a strong positive correlation (regression slope = 0.37, correlation coefficient 0.73) suggesting the foitite substitution $(Al\square)(NaFe^{2+},Mg)_{-1}$. Regression of the data from the tourmaline nodules yielded a weaker but still significant correlation (0.66) and a shallower slope (0.09). The plot of Al $-\square$ against Fe + Mg + $\square$ (Fig. 6h) allows us to separate the effects of deprotonation from the $AlFe_{-1}$ exchange as described above. The Diamante breccia-hosted and nodular tourmaline groups are neatly discriminated on this plot, with deprotonation indicated for the tourmaline breccia and the opposite for the nodules.

In summary, the Al-Fe-Mg variations in nodule-hosted tourmaline can be related to a combination of the foitite and $AlFe_{-1}$ substitutions with little contribution by $MgFe_{-1}$ or deprotonation. In contrast, the $MgFe_{-1}$ substitution was important in the breccia-hosted tourmaline, $AlFe_{-1}$ was insignificant, and the remaining variations reflect combined effects of the foitite and deprotonation substitutions. Most tourmaline grains in the breccia matrix from Diamante are large enough for analysis of core-rim variations. Many grains are unzoned, but consistent core-rim changes in Mg/(Fe + Mg) and Ca/(Ca + Na) were found in several grains from sample RB305. Within-in-grain variations in RB322 are as large as in RB305 (e.g., Mg/Fe + Mg from 0.2 to 0.8), but in this case, the core-rim trends are not consistent from one grain to another.

Boron isotope composition of tourmaline

Boron isotope ratios were determined by SIMS analysis of tourmaline from four samples of mineralized breccias in the mine area, two samples of barren breccia from the Diamante prospect, and two samples of tourmaline nodules in granite from Diamante. The results of 96 analyses, expressed in $\delta^{11}B$ values, are reported in the data publication (Hohf and Trumbull, 2022), and values for selected samples are given on Table 2. Care was taken to check for isotopic zoning, but the small grain size of tourmaline in the mine area samples made that impossible in many cases. Where multiple analyses were made, mostly of tourmaline from Diamante, internal variations were smaller than 2‰, and core-rim trends were either absent or not systematic.

Mine area: Overall, the range of $\delta^{11}B$ in tourmaline from mineralized breccia is from –0.5 to 6.6‰, with an average value of 3.9 ± 1.5‰ (n = 28). In detail, the two localities, La Americana and Sur-Sur, yielded slightly different ranges of $\delta^{11}B$ (Fig. 7). The range for tourmaline from La Americana (sample RB11) is 4.0 to 6.6‰, average 5.5‰, (n = 8), while three samples from Sur-Sur gave consistently lower values as follows; RB231: 3.0 to 5.3‰, average 3.7, n = 6; RB263: 1.8 to 5.1‰, average 3.8, n = 6, one outlier at –0.5‰; and RB269: 2.7 to 3.9‰, average 3.1, n = 8. Thus, the average values of $\delta^{11}B$ from La Americana and Sur-Sur differ by about 2‰. Apart from possible sampling bias (one sample from La Americana vs. three from Sur-Sur), this can be attributed to
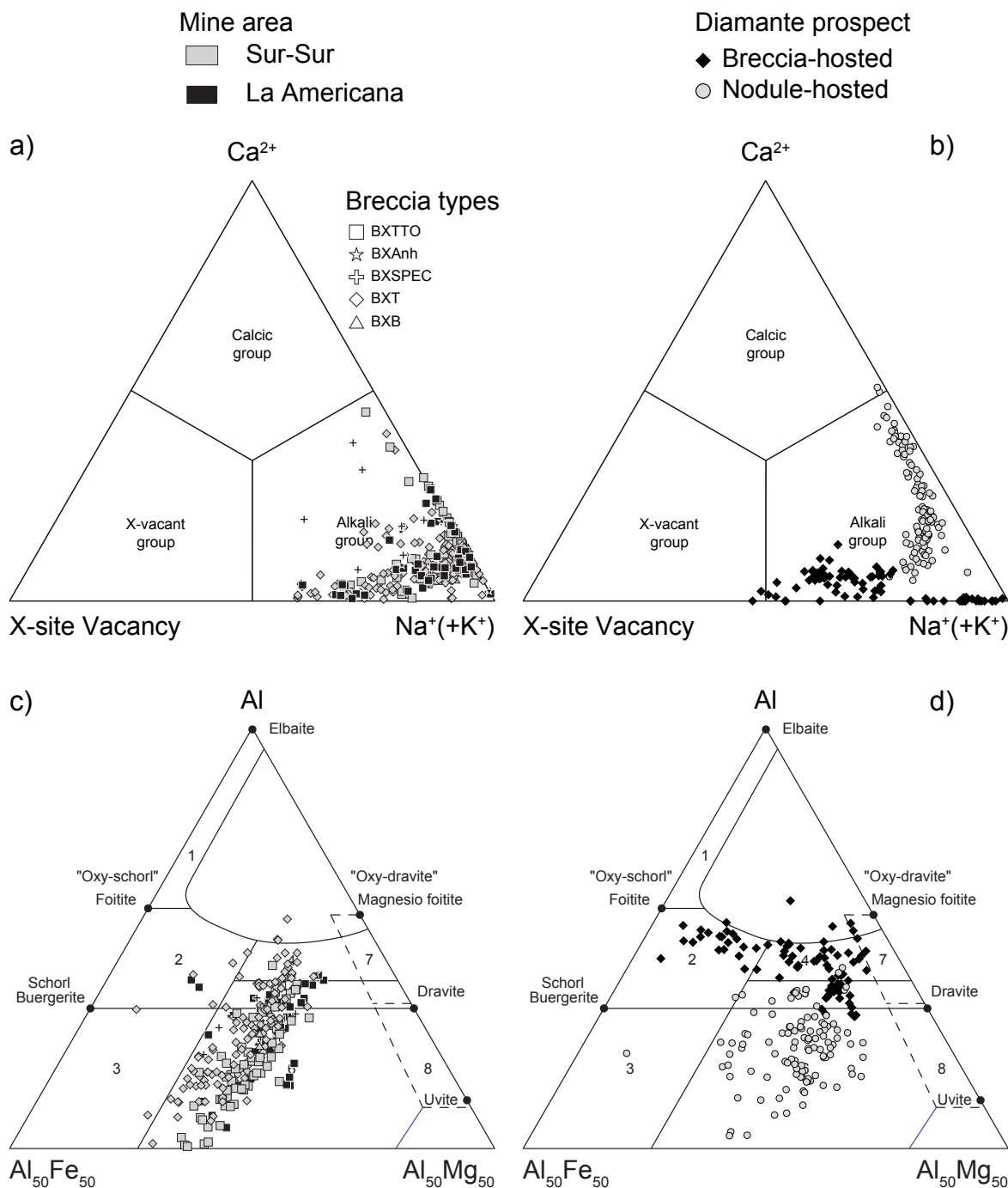
Fig. 5. Tourmaline compositions from the mine area (left) and Diamante prospect (right) on ternary plots of X-site occupancy (a, c) after Henry et al. (2011), and Al-Fe-Mg (b, d) after Henry and Guidotti (1985). Abbreviations: BXAnh = anhydrite breccia, BXB = biotite breccia, BXSPEC = specularite breccia, BXT = tourmaline breccia, BXTTO = tuffaceous tourmaline breccia.

changes in the hydrothermal fluid composition or the temperature of mineralization (or both). More discussion of this point is given in a later section.

Testa (2019) reported B isotope ratios for tourmaline from the La Americana breccia and associated veins (–0.7 to 6.2‰, n = 14). The analyses were done by SIMS without a matrix-matched reference material (NIST 610 glass was used). This is likely to introduce bias in results (Rosner et al., 2008), but

in fact, the data of Testa (2019) agree quite well with our $\delta^{11}B$ values.

Diamante area: The barren breccia samples from Diamante (RB305 and RB322) have overlapping B isotope compositions (5.2 ± 1.8 vs. 4.4 ± 1.7‰, respectively), and the combined average for both is 4.8 ± 1.7‰ (n = 20). The tourmaline nodules from Diamante granite sample RB304 (tourmaline Type 1) yielded $\delta^{11}B$ values from 3.5 to 7.7‰ (avg 5.0 ± 1.3‰,
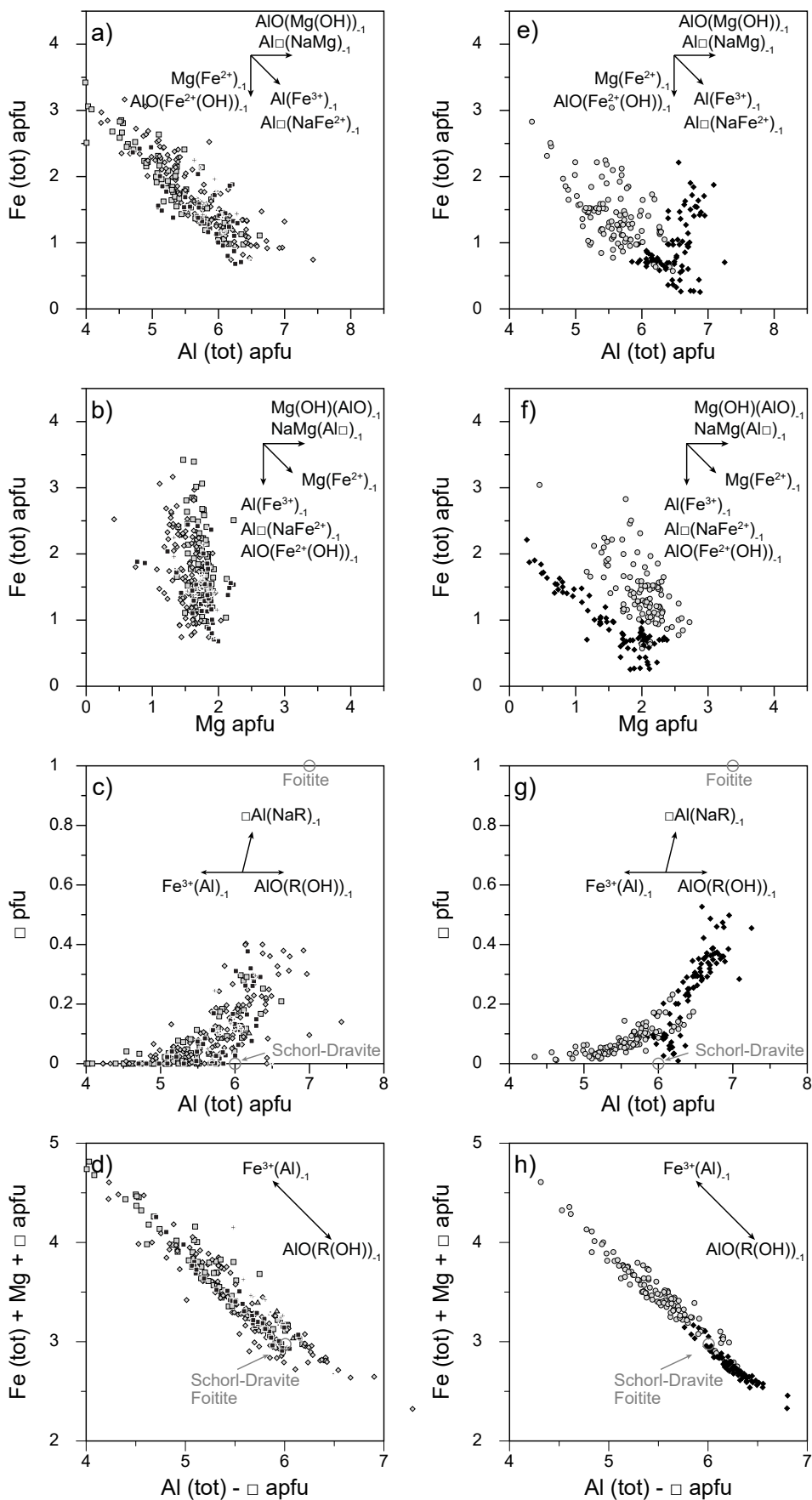
Fig. 6. Tourmaline compositions from the mine area (left) and Diamante prospect (right) on selected binary plots (legend as on Fig. 5) illustrating contrasts in element distribution in tourmaline from the mineralized and barren breccia. Concentrations in atoms per formula unit (apfu); open square denotes X-site vacancy ($\square$). Shown on each plot are possible exchange vectors discussed in the text.
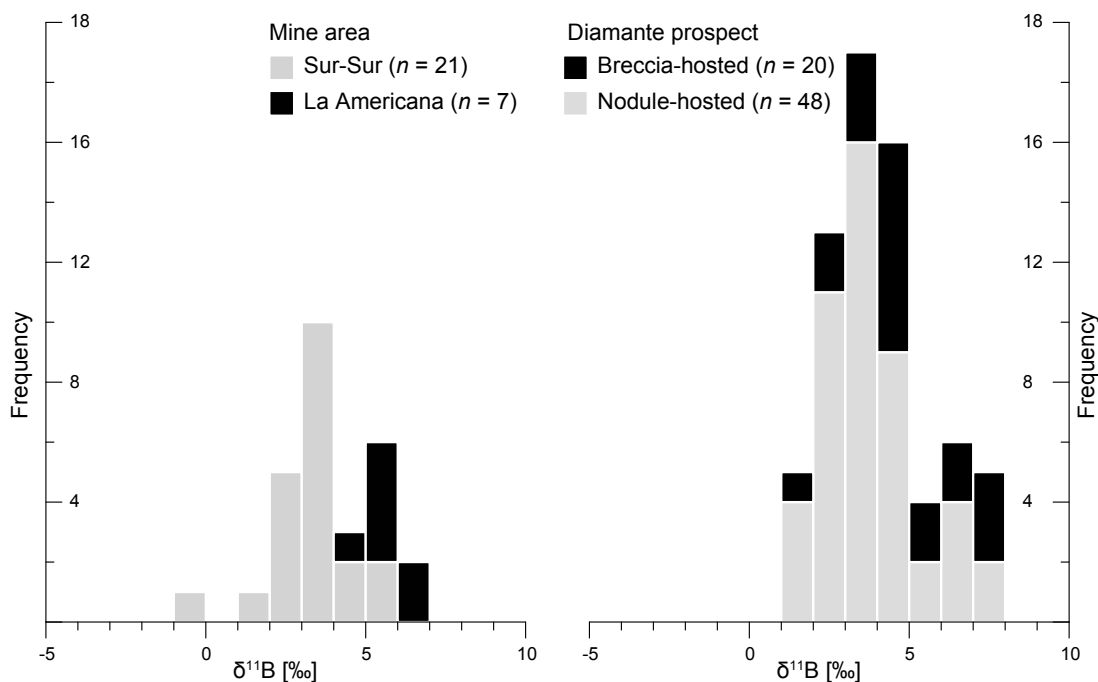
Fig. 7. Frequency histograms of boron isotope ratios in tourmaline samples from the mine area (left) and Diamante prospect (right).

n = 18), which is indistinguishable from the breccia-hosted tourmaline. The second nodular tourmaline sample RB306, which contains both Type 2 and Type 1 tourmaline, yielded an overall range of 1.2 to 4.3‰ with an average of 2.9 ± 0.8‰ (n = 30). The two types of tourmaline in this sample show no significant difference in B isotope composition (see Fig. 4c).

In summary, the $\delta^{11}B$ values of all tourmaline samples in this study fall within the range of about 2 to 8‰, with one outlier at –0.5‰. Within-sample variations are on the order of 2 to 3‰, and the average values of all samples fall in the range from 2.9 to 5.5‰. Tourmaline from mineralized breccia, barren breccia, and granite-hosted nodules defines a frequency maximum at 2 to 6‰ $\delta^{11}B$ (Fig. 7). How this composition relates to possible sources of boron is discussed in a later section, but an important observation is that the nodule-hosted tourmaline from the Diamante granite has essentially the same B isotope composition as tourmaline from the barren hydrothermal breccias associated with it, and also the same as mineralized breccias in the mine area. Whatever the ultimate source of boron was, the equivalence of B isotope composition in hydrothermal and magmatic tourmaline suggests that the hydrothermal fluids were magmatic, which is consistent with the range of I-type magmas (mean –2‰, s.d. 5.2; Trumbull and Slack, 2018, also see discussion section). Furthermore, the equivalence of barren and mineralized breccias in terms of tourmaline $\delta^{11}B$ indicates that boron isotope ratios are not a good indicator of mineralization potential (see discussion).

Sulfur isotope composition of sulfide minerals and anhydrite

The $\delta^{34}S$ values in sulfide and anhydrite mineral separates from eight samples of mineralized breccia and from two crosscutting veins in the mine area are reported on Table 3. No S isotope analyses were made on the barren breccia from the Diamante prospect, which contains only accessory pyrite.

The $\delta^{34}S$ values of chalcopyrite in breccia-hosted samples from Sur-Sur and La Americana are between –2.5 and –0.3‰ (n = 8), and there is no significant difference between the two localities. Other sulfide minerals in the breccia yielded essentially the same $\delta^{34}S$ values as chalcopyrite (molybdenite: –2.2 to –0.2‰; bornite: –2.4‰), while enargite and pyrite from post-breccia veins gave a slightly wider range (–3.9 to 0.5, and 1.0‰, respectively). Anhydrite in breccia samples in both localities yielded a combined range of $\delta^{34}S$ from 9.3 to 14.5‰ (n = 5) with no apparent difference between them. No data exist for the late veins since they lack anhydrite. Coexisting chalcopyrite and anhydrite in four breccia samples where the minerals appear to be in textural equilibrium (RB8 and RB78 from La Americana, RB231 and RB244 from Sur-Sur) yielded values of $\delta^{34}S$ (sulfate-sulfide) from 14.1 to 15.3‰ and 13.4 to 15.8‰, respectively. The corresponding S isotope exchange temperatures based on Ohmoto and Lasaga (1982) are 389° to 419°C for La Americana and 377° to 437°C for Sur-Sur (Table 3). These temperatures are in the mid-range of the 250° to 500°C recorded by quartz-hosted fluid inclusions in the two breccia bodies reported by Vargas et al. (1999) and Frikken et al. (2005). It is impossible to more precisely correlate the fluid inclusion record with sulfide-sulfate crystallization in the breccias, and we can only conclude that the S isotope exchange temperatures appear reasonable for equilibrium between the two phases. Also, the temperatures are in the same range for both the Sur-Sur and La Americana localities.

Discussion

Boron isotope variations and implications for the boron source

Overall, the range of 96 $\delta^{11}B$ values determined in this study range from about 2 to 8‰ (with one outlier at –0.5‰).

Within-sample variations are typically 3‰ or less, and the averages vary from 2.9 to 5.5‰. This is a narrow range, but it was noted above that tourmalines from mineralized breccias in La Americana have slightly higher $\delta^{11}B$ values than in Sur-Sur (Fig. 7). This difference are worth discussion since it could shed light on differences in the temperatures of mineralization and/or compositions of the hydrothermal fluid. The tourmaline-fluid fractionation factors of Meyer et al. (2008) imply that a shift of 2‰ can result from a temperature change of about 200°C, which is well within the range indicated by fluid inclusions studies. However, Vargas et al. (1999) studied fluid inclusions in quartz from both La Americana and Sur-Sur breccias and found the same 250° to 500°C range in each. While it is likely that a temperature range accounts for some of the B isotope variations found within samples, there is no apparent contrast between the two localities that would explain their B isotope difference. Also, the S isotope exchange temperatures estimated from mineral pairs are the same in both localities (Table 3). The possibility remains that hydrothermal fluids in the Sur-Sur and La Americana breccias had different B isotope compositions when tourmaline formed. Assuming, as seems likely, a magmatic source of boron (see below), there is no reason to suggest a difference in magma composition in the two localities. More likely are isotopic shifts in the fluid composition. Minor shifts could result from the magmatic-hydrothermal transition (fluid being enriched in ^{11}B relative to melt) and from the crystallization of hydrothermal tourmaline or micas. Both minerals partition ^{10}B relative to fluid, but the effect of tourmaline is weaker (e.g., 2 vs. 10‰ at 500°C; Kowalski and Wunder, 2018). Biotite and sericite are both locally abundant, but they relate to different alteration stages (potassic and phyllic, respectively), so their timing with respect to tourmaline formation is important. According to Frikken et al. (2005) the biotite-rich breccia zone at Sur-Sur underlies the phyllic zone in which tourmaline occurs. Sericite should play no role if it coprecipitates with tourmaline because of the vastly greater boron concentration in the latter. Conceivably, hydrothermal fluid that precipitated massive biotite in deeper levels of the breccia system might be depleted in ^{10}B before tourmaline crystallized in shallower depth. Like with the temperature effects, it is conceivable that mica crystallization or magma degassing cause isotopic variations in the fluid that contribute to the range of tourmaline composition. However, there is no reason to expect that these processes affected the Sur-Sur and La Americana breccias differently. Given the evidence for multiphase intrusion, fluid production, and brecciation in the Río Blanco-Los Bronces district, the evolution of B isotope ratios in the fluid(s) and in the tourmaline that formed from them cannot be resolved in the scope of our study but would require much more detailed sampling and investigation.

The main features of the B isotope data set that we consider important are the narrow range of $\delta^{11}B$, the positive values, and the similarity of B isotope composition in mineralized breccia, barren breccia, and granite-hosted nodules. It is worth pointing out that this similarity in isotopic composition is in contrast to distinct chemical differences between mineralized and barren breccia samples on the one hand, and to the tourmaline from granite nodules on the other (Fig. 6). An explanation for the independence of chemical and B isotope

variations, and for the much greater homogeneity of the latter, is that boron is a fluid-mobile element not much affected by crystallization of minerals other than tourmaline (or micas in very high modal amounts). In contrast, the major elements in tourmaline also have high concentrations in the host rocks, so their concentrations in hydrothermal fluid and incorporation into tourmaline can be affected by variations in the water/rock ratio and by the growth or dissolution of coexisting minerals including feldspars (Al, Na, Ca), sericite (Al), pyrite, and chalcopyrite (Fe).

A magmatic source of the boron in tourmaline breccias is suggested by the overlap of $\delta^{11}B$ values with tourmaline nodules in the Diamante granite (Fig. 7), which we presume formed from the magma at a late stage of crystallization or possibly in the subsolidus. It should be noted that the Diamante granite is among the oldest units of the San Francisco Batholith (U-Pb zircon age 16.52 ± 0.07 Ma; Hohf, 2021), whereas the porphyry intrusions in the mine area are younger (ca. 9–5 Ma). Skewes and Stern (1995) suggested that the porphyry intrusions hosting mineralization are not cogenetic with the batholith based on Sr-Nd isotope differences. We cannot rule out that the magmatic B isotope composition of Diamante granite and porphyry intrusions differed, but the similarity of tourmaline compositions throughout the district suggests otherwise. In any case, the $\delta^{11}B$ range of breccia-hosted and granite-hosted tourmaline in the Río Blanco-Los Bronces district is well within the range of global I-type magmatic rocks (–10 to 12‰; Trumbull and Slack, 2018), and more direct comparisons can be made with data from Neogene magmatic rocks in the Central Andes. Rosner et al. (2003) reported whole-rock $\delta^{11}B$ values for Neogene andesite and dacites ranging from –7.2 to 4.2‰. That study showed a systematic trend in $\delta^{11}B$ with distance from the trench and, for the frontal arc setting appropriate for the Río Blanco-Los Bronces location, the range is 2 to 4 ‰. In situ analyses of $\delta^{11}B$ in quartz-hosted melt inclusions were made by Schmitt et al. (2002) from dacitic ignimbrites in the Altiplano region, Chile, and by Wittenbrink et al. (2009) from the Eocene El Salvador porphyry in northern Chile. Both studies found a considerable range of $\delta^{11}B$ (–9.7 to 2.5‰ for the ignimbrites, –7 to 12‰ for El Salvador), which the authors attributed to magma mixing of mantle-derived arc magma with isotopically heavy boron and crustal melts with lighter boron. Finally, Tornos et al. (2012) reported tourmaline $\delta^{11}B$ values of –3.1 to –1.4‰ from the Copucha porphyry Cu deposit in northern Chile and concluded a magmatic source. These comparisons suggest that the boron in the Río Blanco-Los Bronces system could be derived from the arc magmas. On the other hand, B isotope values in the range of the Río Blanco-Los Bronces tourmaline can also be explained by assimilation into the magma of marine-derived boron. This could take place either in the mantle wedge source region from slab dewatering (e.g., Rosner et al., 2003; De Hoog and Savov, 2018) or in the upper crust from interaction with Jurassic-Cretaceous carbonate and evaporite rocks that underlie the district (Piquer et al., 2015). To help distinguish a magmatic versus external boron source, two additional aspects are discussed below: data from other stable isotope systems (O-H and S) and a mass balance calculation for boron in the tourmaline breccias.

Oxygen and hydrogen isotopes

Oxygen isotope data are available from Kusakabe et al. (1984) for quartz from mineralized veins in the Río Blanco-Los Bronces district, from Skewes et al. (2003) for tourmaline from the Donoso breccia matrix, and from Frikken (2004) for tourmaline and quartz from the Sur-Sur breccia. All studies used mineral separates for the analyses and the values were reported relative to standard mean ocean water (SMOW). The range of $\delta^{18}O$ for vein quartz is 8.4 to 10.7‰ (avg 9.6 ± 0.8, n = 4), which is essentially the same as quartz from Donoso breccia (6.9 to 10.8‰, avg 9.1 ± 1.8, n = 6). The quartz $\delta^{18}O$ values from Sur-Sur breccia reported by Frikken (2004) are slightly higher (9.7–14.7‰, avg 11.9 ± 1.6, n = 12). From the average $\delta^{18}O$ quartz values of these studies and temperatures of 250° to 500°C from quartz-hosted fluid inclusions (Vargas et al., 1999; Skewes et al., 2003; Frikken et al., 2005), the estimated range of fluid $\delta^{18}O$ is between 0.2 and 9.6‰ according to the quartz-water isotope fractionation equation of Sharp et al. (2016). Tourmaline $\delta^{18}O$ values from the Donoso and Sur-Sur breccias (Skewes et al., 2003; Frikken, 2004, respectively) are nearly the same, with a combined range of 7.5 to 9.0‰. Using the average value of 8.2 ± 0.5 (n = 9) and the tourmaline-water O isotope fractionation equation of Kotzer et al. (1993), the estimated fluid $\delta^{18}O$ range is 3.3 to 8.1‰ for the 250° to 500°C fluid inclusion temperatures.

Hydrogen isotope ratios (δD) of biotite (–70.8 to –85.5‰, avg –81 ± 5.3, n = 5) and sericite (–58.5‰, single analysis) were reported by Kusakabe et al. (1990) from the potassic alteration zone in the Río Blanco deposit. Skewes et al. (2003) determined δD values of –73 to –95‰ (avg –83 ± 9.1) for tourmaline from the Donoso breccia. The corresponding δD_{fluid} estimates using the mineral average values and the 250° to 500°C temperature range are –65 to –12‰ for tourmaline (fractionation equation of Kotzer et al., 1993), –43 to 0‰ for biotite, and –41 to 3.1‰ for sericite (fractionation equation of Suzuoki and Epstein, 1976). It is noted that the cited H isotope fractionation equations were calibrated only above 350°C, so the highest values of δD_{fluid}, which result from 250°C, may be unreliable.

In summary, calculated fluid $\delta^{18}O$ and δD values (relative to SMOW) from available data range from about 0 to 10‰ and –65 to 3‰, respectively, based on the 250° to 500°C range of mineralization temperatures indicated by fluid inclusion studies. This is a broad range, but it is difficult to link particular fluid inclusion temperature ranges (mostly quartz-hosted) with particular mineral isotopic data. For tourmaline, which formed early in the breccia matrix, the high-temperature range of fluid inclusions seems justified (400°–500°C) and the resulting $\delta^{18}O_{fluid}$ and δD_{fluid} values are 6.7 to 8.1‰ and –65 to –51‰, respectively. Skewes et al. (2003) used a wider range of temperatures, from 400° to 690°C, representing the highest reported for quartz-hosted fluid inclusions in their study, to calculate $\delta^{18}O_{fluid}$ and δD_{fluid} values from quartz and tourmaline mineral data. Their estimates are 5.6 to 9.1‰ and –51 to –80‰, respectively. The values are consistent with the range of 5 to 10‰ $\delta^{18}O$ and –40 to –80‰ δD for "primary magmatic water" of Taylor (1979), and this was the conclusion reached by the cited authors. Also, even the broader range of $\delta^{18}O_{fluid}$ and δD_{fluid} calculated for 250° to 500°C and including

biotite and sericite values, contrasts strongly from the composition of meteoric water composition in the Río Blanco-Los Bronces district, which ranges from –16.6 to –15.5‰ $\delta^{18}O$ and –125 to –110‰ δD (Holmgren et al., 1988), so a significant meteoric water input can be ruled out.

Sulfur isotopes

Abundant sulfur isotope ratios of sulfide minerals (mainly chalcopyrite) and anhydrite from the Río Blanco-Los Bronces district have been published (Kusakabe et al., 1984; Holmgren et al., 1988; Frikken et al., 2005). The range of $\delta^{34}S$ values for chalcopyrite from these studies is –4.1 to 3.3‰, average –0.8 ± 1.4‰ (n = 149), and for anhydrite it is 9.9 to 17.9‰, average 12.5 ± 1.7‰ (n = 35). The samples from Sur-Sur and La Americana breccias analyzed in our study yielded $\delta^{34}S$ values of chalcopyrite between –2.5 and –0.3‰ (n = 8) and anhydrite values from 9.3 to 14.5‰ (Table 3), which are in agreement with the previous results. Our data show no apparent difference in S isotope ratios between the two localities.

In a deposit containing both sulfate and sulfide mineral phases, the interpretation of S isotope ratios of the hydrothermal fluid (total sulfur $\delta^{34}S_{fluid}$) depends on the relative proportions of dissolved sulfate/sulfide species. This proportion, and the total sulfur $\delta^{34}S_{fluid}$ value, can be estimated from the mineral compositions provided that (1) the minerals reached and maintained isotopic equilibrium and (2) the sulfate/sulfide ratio as well as the total sulfur $\delta^{34}S$ in the fluid remained constant (e.g., Ohmoto and Rye, 1979; Field et al., 2005; Rye, 2005). Previous workers in the Río Blanco-Los Bronces district disagree as to whether or not chalcopyrite and anhydrite were coeval. Kusakube et al. (1984) concluded that the two minerals coexisted in vein-hosted mineralization at Río Blanco. They derived S isotope exchange temperatures of 400° to 500°C, which are consistent with fluid inclusion data and are in the same range as temperatures calculated from the breccia-hosted anhydrite-chalcopyrite mineral pairs from our study (377°–437°C; Table 3). The paper by Holmgren et al. (1988) does not discuss the paragenetic relationship of sulfide and anhydrite, but the authors used mineral pairs to calculate equilibrium temperatures (450°–600°C), so they were tacitly considered to be cogenetic. Our samples from the Sur-Sur and La Americana breccias contain anhydrite and copper sulfides (chalcopyrite ± bornite) in close textural association without evidence of replacement (Fig. 3e, f), and the agreement between sulfate-sulfide exchange temperatures and fluid inclusion temperatures (although the latter have a wide range) are consistent with isotopic equilibrium. Frikken et al. (2005) stated that anhydrite in the Sur-Sur breccia predated sulfide mineralization, and they did not treat the mineral pairs as cogenetic. We respect this interpretation and do not use their data in the sense of mineral pairs in this paper. However, we note that the $\delta^{34}S$ values of chalcopyrite and anhydrite reported by Frikken et al. (2005) are in the same range as those in our study as well as in Kusakabe et al. (1984) and Holmgren et al. (1988), so the interpretation of total sulfur $\delta^{34}S_{fluid}$ discussed below would be the same with or without the Frikken data set.

Kusakabe et al. (1984) used a graphical method to estimate total sulfur $\delta^{34}S_{fluid}$ from sulfide-sulfate mineral pairs on the so-called "δ–δ plot" illustrated here in Figure 8 with addi-

tional data from Holmgren et al. (1988) and from the present study. If the conditions of mineral equilibrium and closed-system behavior listed above are valid, the sulfate and sulfide data plotted in this way should define two converging linear arrays whose slopes are proportional to the mole fractions of sulfate or sulfide in solution and whose Y-axis intercept gives the total sulfur $\delta^{34}S_{fluid}$ value. In theory, the data on the δ–δ plot should represent the composition of dissolved sulfide and sulfate species. For the sulfate composition, the anhydrite-HSO_4^{2-} fractionation can be ignored (Rye, 2005). For the sulfide component, the fractionation between chalcopyrite and H_2S is –0.18 to –0.08‰ for the temperature range of 250° to 500°C (Ohmoto and Rye, 1979). This fractionation correction is smaller than the uncertainty of the S isotope analyses, but nevertheless, the $\delta^{34}S_{sulfide}$ values on Figure 8 represent the fluid H_2S component, which we calculated for an exemplary temperature of 350°C (fractionation factor = –0.13‰). Plotted in this way, the data from our study combined with those of Kusakabe et al. (1984) and Holmgren et al. (1988) define a total sulfur $\delta^{34}S_{fluid}$ value (Y-axis intercept) of 1.4‰. The uncertainty on this value is 3.9‰ at the 95% confidence limit. A different graphical method described by Rye (2005), which plots $\delta^{34}S_{sulfide}$ against $\delta^{34}S_{sulfate}$, was not applied here because the data do not define a linear trend (correlation coefficient = 0.03). Qualitative approaches to constrain the total sulfur $\delta^{34}S$ from mineral data that do not depend on linear arrays were described by Field et al. (2005) with reference to the Butte porphyry Cu deposit. As a limiting case, one can assume that all magmatic sulfur is present as sulfate, which may be valid for the oxidized arc magmas in the Central Andes where magmatic anhydrite is commonly described (e.g., Chambefort et al., 2008). Following Field et al. (2005), SO_2 will then be the dominant S species in the magmatic fluid phase, which reacts with water to produce a 3:1 ratio of sulfate to sulfide species in the fluid:

$$4SO_2 + 4H_2O = H_2S + 3H_2SO_4. \quad (1)$$
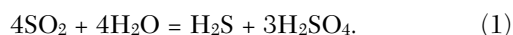
It follows that the mole fractions XSO_4^{2-} and XH_2S in the fluid are 0.75 and 0.25, from which the $\delta^{34}S$ value of total sulfur is calculated from the sulfate and sulfide mineral compositions:

$$\delta^{34}S \text{ (total)} = 0.75 \times (\delta^{34}HSO_4^-) + 0.25 \times (\delta^{34}H_2S). \quad (2)$$

Following Field et al. (2005), the values for $\delta^{34}H_2S$ and $\delta^{34}HSO_4^-$ are taken as the average observed $\delta^{34}S$ of chalcopyrite (corrected to H_2S as described above) and anhydrite (no correction). The averages for the data from this study, Kusakabe et al. (1984), and Holmgren et al. (1988) are –1.6 ± 1‰ and 12.3 ± 1.6‰, respectively, from which the total sulfur composition is calculated as 8.8 ± 1.3‰. Note that this is a maximum value based on the end-member assumption that all magmatic sulfur is oxidized. Field et al. (2005) described an alternative approach that is entirely data based. It relates the observed variation of $\delta^{34}S$ values in sulfide and sulfate minerals to the relative proportion of the respective species in solution. For example, if sulfate were dominant over sulfide in the fluid, the S isotope range of anhydrite will be smaller than that of sulfide minerals, and vice versa. This relation is expressed in equation 10 in Field et al. (2005) given here:

$$XHSO_4^- = \Delta^{34}S_{H_2S} / (\Delta^{34}S_{H_2S} + \Delta^{34}S_{SO_4}) \quad (3)$$

where $XHSO_4^-$ is the mole fraction of sulfate in the fluid, and $\Delta^{34}S_{H_2S}$ or $\Delta^{34}S_{SO_4}$ are the observed ranges of chalcopyrite and anhydrite, respectively. These ranges for the data from this study, Kusakabe et al. (1984), and Holmgren et al. (1988) are 4.7 and 3.5‰, which results in a value for $XHSO_4^-$ of 0.43. Substituting this value for the 0.75 in equation (2) yields an estimate of 4‰ for total sulfur $\delta^{34}S_{fluid}$.

A caveat in all of these approaches is that the ratio of H_2S/SO_4^{2-} in the fluids is assumed to remain constant during mineralization, which the thermodynamic modeling by Hutchinson et al. (2020) suggests is unlikely for most porphyry systems. Indeed, the spatial variations of hematite versus magnetite in the Río Blanco-Los Bronces breccias indicate variable f_{O_2} in the fluid with depth. On the other hand, all samples of tourmaline breccias analyzed in this study originate from the hematite zone or show hematite overprinting magnetite, and consistently oxidizing conditions are confirmed by the Fe^{3+}-Al substitution in tourmaline (Fig. 6a). Subject to the assumptions and qualifications described above, the S isotope data constrain the total sulfur $\delta^{34}S$ values of mineralizing fluid to between 1.4 and 8.8‰. This range extends beyond the mantle values of 0 ± 3‰ (Marini et al., 2011) but is within the broader range of $\delta^{34}S$ in nonmineralized andesites and magnetite-series (I-type) granites compiled by Seal (2006). Therefore, the S isotope composition of sulfide minerals and anhydrite from the Río Blanco-Los Bronces district is consistent with a magmatic source of sulfur, although we do not rule out an external component with higher $\delta^{34}S$ as suggested by Frikken et al. (2005).

A mass-balance assessment of boron in the tourmaline breccias

All stable isotope data described above are permissive of a magmatic source of boron, water, and sulfur in the hydrothermal fluids of the Río Blanco-Los Bronces tourmaline breccias. For boron especially, the equivalence of tourmaline $\delta^{11}B$ values from hydrothermal breccias and from granite-hosted nodules adds support for the magmatic source. An independent test of this is possible because tourmaline is the only important mineral host for boron in the deposit and the 3-D lithologic model of the deposit allows an assessment of the total amount of tourmaline breccia present (mine area only, see Fig. 2). The question addressed with mass balance is whether typical Andean arc magmas can supply the quantity of boron contained in the Río Blanco-Los Bronces tourmaline breccia or if an external source is required. The volume of tourmaline breccia in the mine area from the lithologic model (Codelco-Andina, pers. comm., 2020), combined with an average of 10 vol % of tourmaline in the breccia based on drill core profiles (Fig. 9), yields a value of 220 million tons of tourmaline, or about 7 million tons of boron. This is a considerable underestimate because it does not include the substantial amounts of tourmaline breccia located outside the mine area (e.g., the Los Sulfatos deposit; Fig. 2) nor the amount removed by erosion. Thus, we consider 10 million tons of boron to be a realistic but still conservative estimate for the Río Blanco-Los Bronces system.

A successful model must account for the transport and deposition of at least 10 million tons of boron in the porphyry system. Since the tourmaline breccias are hydrothermal, the

$$y = 0.7829x + 1.4344$$
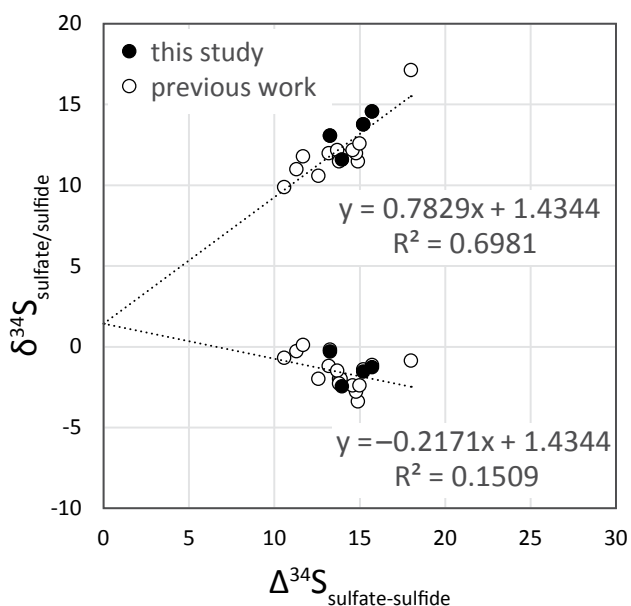$$R^2 = 0.6981$$

$$y = -0.2171x + 1.4344$$
$$R^2 = 0.1509$$

Fig. 8. Plot of sulfur isotope ratios for coexisting sulfate and sulfide phases, after Kusakabe et al. (1984) and Field et al. (2005). Data are from this study and previous work (Kusakabe et al., 1984; Holgrem et al., 1988). Linear regression of anhydrite (upper line) and chalcopyrite data (lower line) defines equations whose slope is equal to the sulfate or sulfide proportion in the system and whose Y-axis intercept represents the total sulfur $\delta^{34}S$ value (see text).
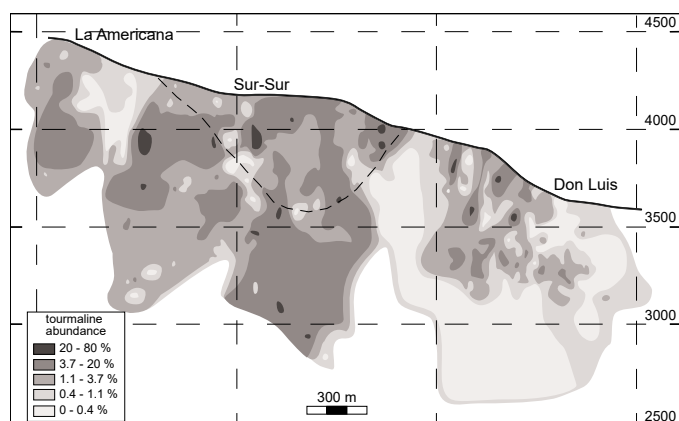
Fig. 9. Tourmaline modal abundance in the La Americana, Sur-Sur, and Don Luis breccias from drill core logs, from Frikken et al. (2005).

model must also consider how much fluid is potentially released by the given amount of magma and the efficiency of boron transfer to the fluid. For this purpose, we modified the petrologic-based mass balance models of Cu endowment in porphyry systems of Chiaradia and Caricchi (2017) and Chiaradia (2020, supplement 2) to work for boron. The modified model is provided in the data publication (Hohf and Trumbull, 2022, table 4). The petrologic framework, from Annen et al. (2006), simulates repeated intrusion of primary arc magmas into the crust, followed by fractionation, variable assimilation of crustal melts, and release of magmatic water. The input data are basal magma flux, depth and lateral extent of the magma accumulation zone, and the initial contents of H_2O in the primary magma and in any crustal melts assimilated.

Also needed are the concentration of boron in the magma and its partition coefficient between fluid and melt ($D^B_{fluid/melt}$). The parameters used are listed and explained on Table 4, whereby the duration of magmatism, water contents, and depth of magma accumulation are allowed to vary randomly within the bounds shown and justified on the table. Various scenarios were modeled (see Hohf and Trumbull, 2022 for all results) using different fixed values of boron concentration in the magma (50 and 75 ppm), different $D^B_{fluid/melt}$ values (1, 3 and 5), and different depth ranges of magma accumulation ("deep" = 7–5 kbar, "shallow" = 3–1 kbar). The depth is important because the pressure-dependent solubility of water in magma determines the amount of fluid that can be released. Results from nine model scenarios are plotted on Figure 10 in terms of the accumulated volume of magma emplaced in the crust (in km³) and the mass of boron (in mT) which can be released from this magma volume to a hydrothermal fluid upon degassing. For each scenario, 1,000 Monte Carlo solutions were calculated. The points on each plot show the 1,000 solutions for a $D^B_{fluid/melt}$ value of 3, and the solid curve tracks the upper bounds for that scenario. Similarly, the dashed and dotted curves in each plot track the upper bounds of 1,000 points calculated for $D^B_{fluid/melt}$ values of 1 and 5, respectively, but individual points are not plotted for clarity (see Hohf and Trumbull, 2022, table 4 for all calculations). The dashed vertical lines on each plot show the accumulated magma volumes in the model after 2 and 4 m.y. given a magma flux of 30 km³/m.y./km arc (Wörner et al., 2018). Four million years is the limit suggested by the age range of porphyry intrusions in the Río Blanco-Los Bronces system.

The importance of $D^B_{fluid/melt}$ in these models is apparent from the solid, dashed, and dotted curves and warrants some discussion. Experimental studies of fluid/melt partitioning at low pressure (1–2 kbar) agree on an enrichment of boron in the fluid, with $D^B_{fluid/melt}$ values between 2 and 3 (Pichavant, 1981; London et al., 1988) or between 1 and 2 (Maner and London, 2018), whereas one study at higher pressure (5 kbar) determined a $D^B_{fluid/melt}$ value of about 1.2 (Hervig et al., 2002). These studies imply that boron partitioning to the fluid is weak to moderate. However, Schatz et al. (2004) investigated boron partitioning among three phases: haplogranite melt, aqueous brine, and vapor at 1 kbar pressure. Their results showed strong partitioning of boron to the vapor phase ($D^B_{fluid/melt}$ = 5) and subequal concentrations in the melt and brine phases. This suggests effective vapor-phase transport of boron in the case of shallow-level degassing, and we recall the fluid inclusion evidence of boiling in the Río Blanco-Los Bronces breccia system described above. Important empirical evidence for strong boron partitioning to magmatic fluid comes from analysis of coexisting fluid and melt inclusions in granitic quartz ($D^B_{fluid/melt}$ = 8 to 18: Audétat and Pettke, 2003; 2 to 20: Zajacz et al., 2008; and 3 to 6: Audétat et al., 2008).

Figure 10A represents a scenario typical for the Neogene Andean volcanic arc, with a magmatic boron concentration of 50 ppm based on studies of volcanic rocks and melt inclusions, and a level of intrusion from 15 to 20 km based on geophysical indications of midcrustal magma accumulation under the Altiplano-Puna plateau region (see Table 4 for references). The modeling shows that the target 10 mT of boron is achieved in rare, extreme solutions for $D^B_{fluid/melt}$ = 3 (solid

Table 4. Input Values for Boron Mass-Balance Modeling

Duration of intrusion	0 to 4 m.y.
Pressure of intrusion	7 to 5 kbar (deep) and 3 to 1 kbar (shallow)
Intrusion column and flux	2.5 km radius, 7.5 km/m.y.
H_2O content mafic magma/crust	2 to 4 wt %/0.2 to 1 wt %
Boron concentration in magma	50 and 75 ppm
Values of boron $D_{fluid/melt}$	1, 3, and 5

The duration of magmatism of 0 to 4 million years after first emplacement is based on porphyry ages in the Río Blanco-Los Bronces district (8.5–5.0 Ma discounting the postmineral La Copa complex; Toro et al., 2012); the pressure range of magma emplacement in the crust is 8 to 5 kbar based on the 20- to 15-km depth of intracrustal magma bodies below the Altiplano-Puna plateau (e.g., de Silva and Kay, 2018); the lateral dimension of the intrusion column is a disk of 2.5 km radius, equivalent to the size of the mine area at surface; the rate of intrusion is 7.5 km/m.y. to match a "basal arc flux" for the Central Andes of 30 km^3/m.y./km arc length (Wörner et al., 2018); the initial H_2O contents for primary magmas and crustal rocks are allowed to vary from 2 to 4 wt % and from 0.2 to 1 wt %, respectively, as in Chiaradia (2020); the B concentration of 50 ppm is based on data from Cenozoic volcanic rocks in Chile (Rosner et al., 2003, avg 27 ± 18, n = 19), from quartz-hosted melt inclusions in dacite from Chile (Schmitt et al., 2002, avg 54 ± 13, n = 30), and from quartz-hosted melt inclusions in porphyry intrusions at Llallagua, Chorolque, and El Salvador (Wittenbrink et al., 1999, avg 60 ± 25, n = 15); results are also shown for elevated boron concentration of 75 ppm

curve and points); all calculations for $D_{fluid/melt}$ = 1 fall short (dashed curve), but for $D_{fluid/melt}$ = 5 (dotted curve) the target is reached after about 350 km^3 of magma accumulation. Scenario B (Fig. 10B) represents the same conditions as scenario A, except for a 50% increase in the amount of boron in the magma (75 ppm) relative to the existing estimates for normal Andean arc magma (see Table 4). In this case, the model for $D^B_{fluid-melt}$ = 3 reaches the target of 10 Mt in many simulations after about 400 km^3, solutions for $D^B_{fluid-melt}$ = 1 still fall far short, and the model for $D_{fluid/melt}$ = 5 requires only 250 km^3 or about 2 m.y. of magmatic activity to produce 10 Mt of boron in the fluid. Scenario C (Fig. 10C) considers the elevated boron concentration of 75 ppm in the magma, but in this case, magma accumulated in a shallow level (3–1 kbar). Under these conditions, none of the model solutions reach the target 10 Mt. The reason is the much lower water solubility in the magma at low pressure, meaning that there is insufficient fluid released to transport boron even for $D_{fluid/melt}$ = 5.

The mass balance modeling clearly oversimplifies a complex system, but the results suggest that the estimated 10 Mt of boron present in the Río Blanco-Los Bronces tourmaline breccias could be produced by typical Central Andes arc magmatism (50 ppm B concentration, 30 km^3/m.y./km arc flux) within the time frame of 4 m.y. if two conditions are met. First, the level of magma accumulation must be deep enough (15–20 km) to maintain a high water solubility in the melt; and second, when hydrous porphyry magmas ascended from the accumulation zone and degassed at shallower levels, the $D^B_{fluid-melt}$ value must have been considerably higher than 3. The first condition is consistent with the concept of transcrustal magmatic systems in continental arcs (e.g., Annen et al., 2006; Cashman et al., 2017) and with direct geophysical and petrologic evidence for magma accumulation at 10- to 30-km depth in the Central Andes (e.g., Risse et al., 2013; Ward et al., 2017; de Silva and Kay, 2018). The condition of high $D^B_{fluid-melt}$ values finds support in melt-vapor partitioning
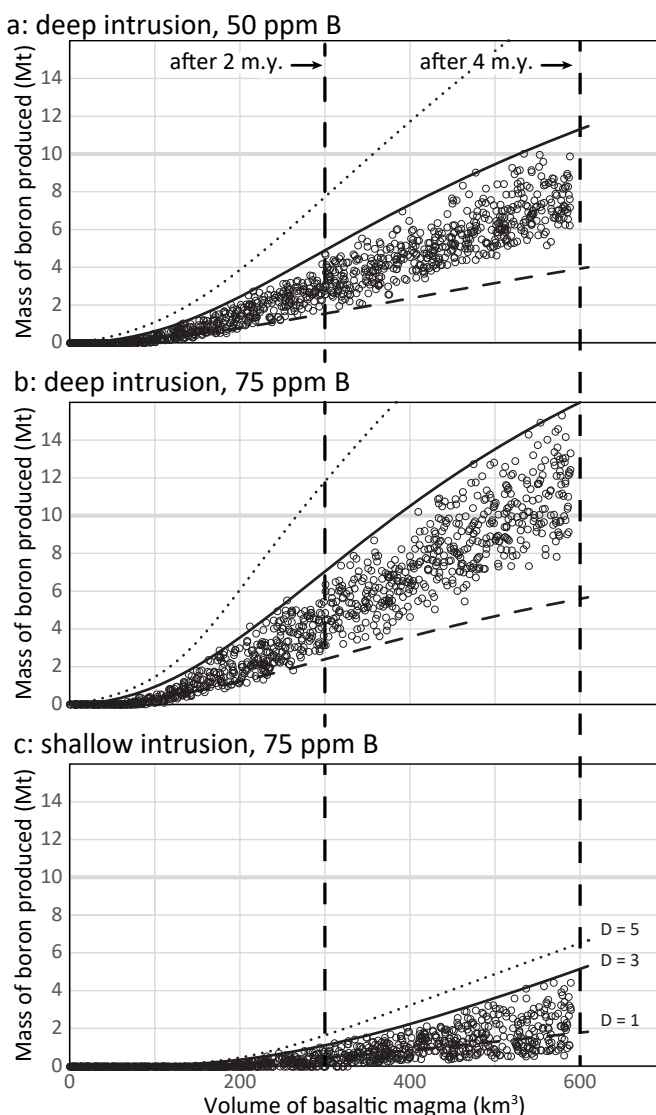

Fig. 10. Mass-balance simulations of a magmatic model for boron in the Río Blanco-Los Bronces tourmaline breccias adapted from the Monte Carlo approach of Chiaradia (2020), with input parameters on Table 4. The X-axis shows the magma volume accumulated for up to 4 m.y. of arc activity in cubic kilometers, and the Y-axis gives the mass of boron released to a fluid phase in megatons. Three scenarios (a, b, c) explore different depths of magma accumulation and boron concentrations in the magma, each calculated with three values of the fluid/melt distribution coefficient for boron (1, 3, 5, see bottom panel). In each panel, the gray horizontal line is the model target: 10 Mt of boron contained in tourmaline breccias from the mine area. Circles are 1,000 simulations using a fluid/melt distribution coefficient of 3; solid curve is the upper bound of those simulations. Dashed and dotted curves represent the upper bounds of 1,000 simulations for D-values of 1 and 5, respectively (see text for discussion).

experiments by Schatz et al. (2004) and empirical studies of trapped melt and fluid inclusions, some of which represent porphyry Cu and Mo systems (Audétat et al., 2008). The alternative to high $D^B_{fluid-melt}$ would be higher initial boron concentrations in the parental magma. The scenario in Figure 10B invokes a 50% increase in boron over what we consider typical for the Central Andes arc. About two-thirds of the Monte Carlo simulations using $D^B_{fluid-melt}$ = 3 reach the target of 10 Mt boron in the 4-m.y. time limit. Given the positive $\delta^{11}B$

values of the Río Blanco-Los Bronces tourmaline (and calculated fluid), any additional, external boron must also be isotopically heavy, which rules out the Andean basement (–15 to –5‰, Kasemann et al., 2000). Possible boron sources could be serpentinite in the mantle wedge or Mesozoic marine sedimentary rocks in the upper crust beneath the district (Piquer et al, 2015). However, it is hard to reconcile the amount of assimilation needed to raise the boron concentration in the magma by 50% with the magmatic signature of O, H, and S isotopes in the breccia-hosted mineralization. The simpler solution to satisfy the mass-balance constraints is to assume strong partitioning of boron to the fluid, with $D^B_{fluid-melt}$ values on the order of 5 or more. If, as suggested by Schatz et al. (2004), this implies vapor-phase transport, that would be consistent with fluid inclusion evidence of boiling conditions (e.g., Frikken et al., 2005), and it might help explain why tourmaline is abundant only in shallow levels of the Río Blanco-Los Bronces breccias but gives way to biotite below a few hundred meters.

Comparison of mineralized and barren breccias and implications for exploration

The boron isotope compositions of tourmaline from mineralized (mine area) and barren breccias (Diamante) are essentially the same, so at least in this district, B isotope ratios are a poor indicator of mineralization potential. On the other hand, the chemical variations of tourmaline do show systematic differences between the mine area and Diamante prospect. The contrast is clear in the Al-Mg-Fe ternary plot, where tourmaline from the barren breccias plots above and parallel to the schorl-dravite join with highly variable Mg/Fe but rather constant Al (Fig. 5d), whereas tourmaline in all samples of mineralized breccias (n = 271 analyses) plots along a "povondraite-oxydravite" trend extending from above the schorl-dravite join to lower Al (Fig. 5c). Furthermore, the strong negative correlation of Al and Fe in these samples (Fig. 6a) suggests that the Al is substituted by Fe^{3+}. In contrast, the negative correlation of Mg and Fe in tourmaline from barren breccias (Fig. 6f) suggests a monovalent exchange of Fe^{2+} and Mg. Other factors besides oxygen fugacity can influence the Fe-Mg-Al distribution in tourmaline, but the distribution of hematite vs. magnetite in the Sur-Sur breccia indicates local redox changes. Frikken et al. (2005) showed that hematite dominates over magnetite in the upper parts of the Sur-Sur breccia generally. In drill core TSS-22, from which our samples RB231 and RB240 derive, the hematite-magnetite boundary is at about 3,350 m according to Frikken et al. (2005). The position of RB231 (3,362 m) is in the hematite zone, whereas RB240 (3,236 m) is below it. The lowest Al and highest Fe contents in tourmaline from the magnetite-bearing sample RB240 are 5.6 and 1.6 apfu, respectively. Contents of Al are much lower, and Fe correspondingly higher, in the hematite-zone sample RB231 (4.2 and 3.0, respectively), in keeping with a greater proportion of ferrous iron in the latter. Similar features of Fe-Al relations in tourmaline have been noted in porphyry deposits worldwide and interpreted as an indicator of oxidizing fluid (Slack, 1996; Baksheev et al., 2012). Beckett-Brown et al. (2021) evaluated tourmaline compositions in bedrock and surficial deposits in and around the Casino and Woodjam porphyry deposits in British Columbia, concluding that the

"povondraite-oxydravite" trend is among the positive traits of tourmaline from mineralized systems. These studies and our results from the Río Blanco-Los Bronces district suggest that Al concentrations significantly below the schorl-dravite value of 6 apfu can be an indicator for mineralization potential, but there must also be a good correlation with Fe conforming to the $Fe^{3+}Al_{-1}$ exchange (Baksheev et al., 2012). For example, our analyses of tourmaline from the granite nodules in Diamante, which have no copper mineralization, show Al contents below the schorl-dravite 6 apfu (Fig. 5d), but in this case, the Fe-Al correlation is weak, indicating that substitutions other than with ferric iron much compensate for the Al deficiency (e.g., $NaR^{2+}(Al\square)_{-1}$, where R can be Fe or Mg; cf. Fig. 6e, g). Finally, it is worth mention that trace element data in tourmaline can help distinguish mineralized settings (although mica proved more effective for this in a comparative study of tourmaline and white mica by Codeço et al., 2021). Trace elements were not analyzed in this study because of the small grain size and complex intergrowths with other minerals. However, Testa (2019) reported LA-ICP-MS analyses of tourmaline from the Río Blanco-Los Bronces district and compared data from mineralized samples (La Americana breccia) with a nonmineralized sector north of the mine area (Las Areneras). The author found that As and Sb performed well as indication for mineralization, while Cu concentrations were variable and showed considerable overlap.

Conclusions

The supergiant Río Blanco-Los Bronces Cu-Mo porphyry district contains one of the world's largest known concentrations of copper, a large proportion of which is hosted in tourmaline-cemented hydrothermal breccias. Tourmaline major element composition and B isotope ratios were determined in 16 samples representing both mineralized (mine area, Sur-Sur and La Americana breccias) and barren tourmaline breccia along with tourmaline-quartz nodules in granite (Diamante prospect area). Tourmaline from mineralized breccias is distinguished by variable Al contents and a strong negative Fe-Al correlation that suggests the substitution $Fe^{3+}Al_{-1}$ and implies oxidizing conditions. These compositions define a trend between the magnesiofoitite/oxydravite and povondraite endmembers on a ternary Fe-Mg-Al plot, which is not the case for tourmaline from barren breccias and granite-hosted tourmaline nodules in the Diamante area. Such "povondraite-oxydravite trends" in tourmaline have been found in many other porphyry Cu deposits worldwide and are suggested as an exploration criterion for mineralized systems that contain tourmaline.

In contrast to the chemical variations, the $\delta^{11}B$ range in tourmaline from mineralized breccias (–0.5 to 6.6‰), barren breccias (1.9–7.9‰), and granite-hosted nodules (1.2–7.7‰) are the same within analytical uncertainty. This similarity indicates that B isotope ratios in tourmaline have no diagnostic power as pathfinder to ore in the Río Blanco-Los Bronces district. In terms of boron source, the positive $\delta^{11}B$ values are compatible with an I-type, arc-related magma with isotopically heavy boron derived from subducted, sea-floor–altered oceanic crust, and there is good agreement between the $\delta^{11}B$ values from Río Blanco-Los Bronces tourmaline determined here and published estimates of magmatic $\delta^{11}B$ values from

the Central Andes. Estimates of total sulfur $\delta^{34}S_{fluid}$ values, derived in different ways from analyses of coexisting chalcopyrite and anhydrite, range from 1.4 ± 3.9 to 8.8 ± 1.3‰. These estimates are to some extent model dependent and are not well constrained because of the spread of mineral compositions and mineralization temperature. Nevertheless, they are consistent with an arc magmatic source according to literature compilations by Seal (2006), and there is further support for a magmatic fluid given by oxygen and hydrogen isotope ratios of breccia-hosted quartz and tourmaline (Holmgren et al., 1988; Skewes et al., 2003). Therefore, a magmatic scenario is permitted by all stable isotope evidence, and this scenario was tested for consistency with the huge amount of tourmaline hosted in Río Blanco-Los Bronces breccias using stochastic mass-balance calculations for boron coupled with a petrologic model of arc magmatism (Chiaradia, 2020). Lithologic models of the deposit coupled with tourmaline modal abundance from drill core logging suggest about 10 mT of boron are contained in the mine area. The modeling shows that this amount of boron can be supplied by arc magmas under conditions typical for the Central Andes (30 km³/m.y./km magma flux, 2–4 wt % H_2O, 50 ppm B), provided that magma accumulates in midcrustal depths before ascent of individual porphyry intrusions, and that boron strongly partitions into the fluid phase upon degassing ($D^B_{fluid-melt} >> 3$).

Acknowledgments

REFERENCES

Annen, C., Blundy, J.D., and Sparks, R.S.J., 2006, The genesis of intermediate and silicic magmas in deep crustal hot zones: Journal of Petrology, v. 47, p. 505–539.

Audétat, A., and Pettke, T., 2003, The magmatic-hydrothermal evolution of two barren granites: A melt and fluid inclusion study of the Rito del Medio and Cañada Pinabete plutons in northern New Mexico (USA): Geochimica et Cosmochimica Acta, v. 67, p. 97–121.

Audétat, A., Pettke, T., Heinrich, C.A., and Bodnar, R.J., 2008, The composition of magmatic-hydrothermal fluids in barren and mineralized intrusions: Economic Geology, v. 103, p. 877–908.

Baksheev, I.A., Prokof'ev, V.Y., Zaraisky, G.P., Chitalin, A.F., Yapaskurt, V.O., Nikolaev, Y.N., Tikhomirov, P.L., Nagornaya, E.V., Rogacheva, L.I., Gorelikova, N.V., and Kononov, O.V., 2012, Tourmaline as a prospecting guide for the porphyry-style deposits: European Journal of Mineralogy, v. 24, p. 957–979.

Beckett-Brown, C.E., McDonald, A.M., McClenaghan, M.B., Plouffe, A., and Ferbey, T., 2021, Investigation of tourmaline characteristics in bedrock and surficial sediment samples from two Canadian porphyry copper systems, in Schetselaar, E., and Plouffe, A., eds., Targeted Geoscience Initiative 5: Contributions to the understanding and exploration of porphyry deposits: Geological Survey of Canada, Bulletin, v. 616, p. 109–135.

Cashman, K.V., Sparks, R.S.J., and Blundy, J.D., 2017, Vertically extensive and unstable magmatic systems: A unified view of igneous processes: Science, v. 355, article 6331, doi: 10.1126/science.aag3055.

Catanzaro, E.J., Champion, C.E., Garner E.L., Marienko, O., Sappenfield, K.M., and Shields, W.R., 1970, Boric acid: Isotopic and assay standard reference materials: United States National Bureau of Standards, Special Publication 216-17, 70 p.

Chambefort, I., Dilles, J.H., and Kent, A.J.R., 2008, Anhydrite-bearing andesite and dacite as a source for sulfur in magmatic-hydrothermal mineral deposits: Geology, v. 36, p. 719–722.

Chiaradia, M., 2020, How much water in basaltic melts parental to porphyry copper deposits?: Frontiers in Earth Science, v. 8, p. 138, doi: 10.3389/feart.2020.00138.

Chiaradia, M., and Caricchi, L., 2017, Stochastic modelling of deep magmatic controls on porphyry copper deposit endowment: Scientific Reports, v. 7, article 44523.

Codeço, M.S., Weis, P., Trumbull, R.B., Van Hinsberg, V., Pinto, F., Lecumberri-Sanchez, P., and Schliecher, A.M., 2021, The imprint of ore-forming fluids on trace element contents in white mica and tourmaline from the Panasqueira W-Sn-Cu deposit, Portugal: Mineralium Deposita, v. 56, p. 481–508.

Deckart, K., Clark, A.H., Aguilar, C.A., Vargas, R.R., Bertens, A.N., Mortensen, J.K., and Fanning, M., 2005, Magmatic and hydrothermal chronology of the giant Río Blanco porphyry copper deposit, central Chile: implications of an integrated U-Pb and ⁴⁰Ar/³⁹Ar database: Economic Geology, v. 100, p. 915–934.

Deckart, K., Clark, A.H., and Cuadra, P., 2013, Refinement of the time-space evolution of the giant Mio-Pliocene Río Blanco-Los Bronces porphyry Cu-Mo cluster, Central Chile: New U-Pb (SHRIMP II) and Re-Os geochronology and ⁴⁰Ar/³⁹Ar thermochronology data: Mineralium Deposita, v. 48, p. 57–79.

Deckart, K., Silva, W., Spröhnle, C., and Vela, I., 2014, Timing and duration of hydrothermal activity at the Los Bronces porphyry cluster: An update: Mineralium Deposita, v. 49, p. 535–546.

De Hoog, J.C.M., and Savov, I.P., 2018, Boron isotopes as a tracer of subduction zone processes, in Marschall, H.R., and Foster, G.L., eds., Advances in isotope geochemistry: Boron isotopes: The fifth element: Heidelberg, Berlin, Springer-Verlag, p. 217–247.

De Silva, S.L., and Kay, S.M., 2018, Turning up the heat: High-flux magmatism in the Central Andes: Elements, v. 14, p. 245–250.

Dyar, M.D., Wiedenbeck, M., Robertson, D., Cross, L.R., Delaney, J.S., Ferguson, K., Francis, C.A., Grew, E.S., Guidotti, C.V., Hervig, R.L., Hughes, J.M., Husler, J., Leeman, W., McGuire, A.V., Rhede, D., Rothe, H., Paul, R.L., Richards, I., and Yates, M., 2001, Reference minerals for the microanalysis of light elements: Geostandards and Geoanalytical Research, v. 25, p. 441–463.

Field, C.W., Zhang, L., Dilles, J.H., Rye, R.O., and Reed, M.H., 2005, Sulfur and oxygen isotopic record in sulfate and sulfide minerals of early, deep, pre-Main Stage porphyry Cu-Mo and late Main Stage base-metal mineral deposits, Butte district, Montana: Chemical Geology, v. 215, p. 61–93.

Frikken, P.H., 2004, Breccia-hosted copper-molybdenum mineralization at Río Blanco, Chile: Ph.D dissertation, Hobart, Tasmania, University of Tasmania, 290 p.

Frikken, P.H., Cooke, D.R., Walshe, J.L., Archibald, D.A., Skarmeta, J., Serrano, L., and Vargas, R.A., 2005, Mineralogical and isotopic zonation in the Sur-Sur tourmaline breccia, Río Blanco-Los Bronces Cu-Mo deposit, Chile: Implications for ore genesis: Economic Geology, v. 100, p. 935–961.

Henry, D.J., and Guidotti, C.V., 1985, Tourmaline as a petrogenetic indicator mineral: An example from the staurolite-grade metapelites of NW Maine: American Mineralogist, v. 70, p. 1–15.

Henry, D.J., Novák, M., Hawthorne, F.C., Ertl, A., Dutrow, B.L., Uher, P., and Pezzotta, F., 2011, Nomenclature of the tourmaline-supergroup minerals: American Mineralogist, v. 96, p. 895–913.

Hervig, R.L., Moore, G.M., Williams, L.B., Peacock, S.M., Holloway, J.R., and Roggensack, K., 2002, Isotopic and elemental partitioning of boron between hydrous fluid and silicate melt: American Mineralogist, v. 87, p. 769–774.

Hohf, M., 2021, Magmatic-hydrothermal events, mineralogy and geochemistry of tourmaline breccia in the giant Río Blanco-Los Bronces porphyry copper deposit, central Chile: Ph.D. dissertation, Freiberg, Germany, Technsche Universitäty Bergakademie Freiberg, 136 p.

Hohf, M., and Trumbull, R.B., 2022, Chemical (EPMA) and boron isotope (SIMS) analyses on tourmaline breccias from the Río Blanco-Los Bronces porphyry copper district, Chile: GFZ Data Services, doi: 10.5880/GFZ.3.1.2022.002.

Holmgren, C., Marti, M., Skewes, M.A., Schneider, A., and Harmon, R., 1988, Análisis isotópicos y de inclusiones fluídas en el yacimiento Los Bronces, Chile central: Congreso Geológico Chileno, no. 5, Actas, v. 1, p. B299–B314.

Hutchinson, W., Finch, A.A., and Boyce, A.J., 2020, The sulfur isotope evolution of magmatic-hydrothermal fluids: Insights into ore-forming processes: Geochimica et Cosmochimica Acta, v. 288, p. 176–198.

Irarrázaval, V., Sillitoe, R., Wilson, A., Toro, J., and Lyell, G., 2010, Discovery history of a giant, high grade, hypogene porphyry copper-molybdenum deposit at Los Sulfatos, Los Bronces-Río Blanco district, central Chile: Society of Economic Geologists, Special Publication no. 15, p. 253–269.

Kasemann, S., Erzinger, J., and Franz, G., 2000, Boron recycling in the continental crust of the central Andes from the Palaeozoic to Mesozoic, NW Argentina: Contributions to Mineralogy and Petrology, v. 140, p. 328–343.

Kay, S.M., and Mpodozis, C., 2001, Central Andean ore deposits linked to evolving shallow subduction systems and thickening crust: GSA Today, v. 11, p. 4–9.

Kay, S.M., Mpodozis, C., and Coira, B., 1999, Magmatism, tectonism and mineral deposits of the Central Andes (22°–33°S latitude): Society of Economic Geologists, Special Publication no. 7, p. 27–59.

Kotzer, T.G., Kyser, T.K., King, R.W., and Kerrich, R., 1993, An empirical oxygen- and hydrogen-isotope geothermometer for quartz-tourmaline and tourmaline-water: Geochimica et Cosmochimica Acta, v. 57, p. 3421–3426.

Kowalski, P.M., and Wunder, B., 2018, Boron isotope fractionation among vapor–liquids–solids–melts: experiments and atomistic modeling, in Marschall, H.R. and Foster, G.L., eds., Advances in isotope geochemistry: Boron isotopes: The fifth element, v.7: Berlin-Heidelberg, Springer-Verlag, p. 33–69.

Kusakabe, M., Nakagawa, S., Hori, M., Matsuhisa, Y., Ojeda Figueroa, J.M., and Serrano, L., 1984, Oxygen and sulfur isotopic compositions of quartz, anhydrite and sulfide minerals from the El Teniente and Rio Blanco porphyry copper deposits, Chile: Bulletin of the Geological Survey of Japan, v. 35, p. 583–614.

Kusakabe, M., Hori, M., and Matsuhisa, Y., 1990, Primary mineralization-alteration of the El Teniente and Río Blanco porphyry copper deposits Chile. Stable isotopes, fluid inclusions and $Mg^{2+}/Fe^{2+}/Fe^{3+}$ ratios of hydrothermal biotite, in Herbert, H.K., and Ho, S.E., eds., Stable isotopes and fluid processes in mineralization: University of Western Australia, Publication 2, p. 244–259.

London, D., Hervig, R.L., and Morgan, G.B., VI, 1988, Melt-vapor solubilities and elemental partitioning in peraluminous granite-pegmatite systems: Experimental results with Macusani glass at 200 MPa: Contributions to Mineralogy and Petrology, v. 99, p. 360– 373.

Maner, J.L., IV, and London, D., 2018, Fractionation of the isotopes of boron between granitic melt and aqueous solution at 700°C and 800°C (200 MPa): Chemical Geology, v. 489, p. 16–27.

Marini, L., Moretti, R., and Accornero, M., 2011, Sulfur isotopes in magmatic-hydrothermal systems, melts, and magmas: Reviews in Mineralogy & Geochemistry, v. 73, p. 423–492.

Medaris, L.G., Jr., Fournelle, J.H., and Henry, D.J., 2003, Tourmaline-bearing quartz veins in the Baraboo quartzite, Wisconsin: Occurrence and significance of foitite and "oxy-foitite": The Canadian Mineralogist, v. 41, p. 749–758.

Meyer, C., Wunder, B., Meixner, A., Romer, R.L., and Heinrich, W., 2008, Boron-isotope fractionation between tourmaline and fluid: An experimental re-investigation: Contributions to Mineralogy and Petrology, v. 156, p. 259–267.

Ohmoto, H., and Lasaga, A.C., 1982, Kinetics of reactions between aqueous sulfates and sulfides in hydrothermal systems: Geochimica et Cosmochimica Acta, v. 46, p. 1727–1745.

Ohmoto, H., and Rye, R.O., 1979, Isotopes of sulphur and carbon, in Barnes, H.L., ed., Geochemistry of hydrothermal ore deposits, 2nd ed.: Wiley Interscience, New York, p. 509–567.

Pichavant, M., 1981, An experimental study of the effect of boron on a water saturated haplogranite at 1 kbar vapour pressure: Contributions to Mineralogy and Petrology, v. 76, p. 430–439.

Piquer, J., Skarmeta, J., and Cooke, D.R., 2015, Structural evolution of the Río Blanco-Los Bronces district, Andes of central Chile: Controls on stratigraphy, magmatism, and mineralization: Economic Geology, v. 110, p. 1995–2023.

Risse, A., Trumbull, R.B., Kay, S.M., Coira, B., and Romer, R.L., 2013, Petrology of late Neogene mafic volcanism in the southern Puna Plateau, Argentina: Insights on the source, generation and evolution of mantle melts in a back-arc setting: Journal of Petrology, v. 54, p. 963–1995.

Rosner, M., Erzinger, J., Franz, G., and Trumbull, R.B., 2003, Slab-derived boron isotope signatures in arc volcanic rocks from the Central Andes and evidence for boron isotope fractionation during progressive slab dehydration: Geochemistry, Geophysics, Geosystems, v. 4, p. 9005, doi: 10.1029/2002GC000438.

Rosner, M., Wiedenbeck, M., and Ludwig, T., 2008, Composition-induced variations in SIMS instrumental mass fractionation during boron isotope ratio measurements of silicate glasses: Geostandards and Geoanalytical Research, v. 32, p. 27–38.

Rye, R.O., 2005, A review of the stable-isotope geochemistry of sulfate minerals in selected igneous environments and related hydrothermal systems: Chemical Geology, v. 215, p. 5–36.

Schatz, O.J., Dolejš, D., Stix, J., Williams-Jones, A.E., and Layne, G.D., 2004, Partitioning of boron among melt, brine and vapor in the system haplogranite-H_2O-NaCl at 800°C and 100 MPa: Chemical Geology, v. 210, p. 135–147.

Schmitt, A.K., Kasemann, S., Meixner, A., and Rhede, D., 2002, Boron in central Andean ignimbrites: Implications for crustal boron cycles in an active continental margin: Chemical Geology, v. 183, p. 333–347.

Seal, R.R., II, 2006, Sulfur isotope geochemistry of sulfide minerals: Reviews in Mineralogy and Geochemistry, v. 61, p. 633–677.

SERNAGEOMIN, 2002, Mapa Geológico de Chile, escala 1:1.000.000: Serie Geológia Básica Nr. 75, Santiago, Chile.

Sharp, Z.D., Gibbons, J.A., Maltsev, O., Atudorei, V., Pack, A., Sengupta, S., Shock, E.L., and Knauth, L.P., 2016, A calibration of the triple oxygen isotope fractionation in the SiO_2-H_2O system and applications to natural samples: Geochimica et Cosmochimica Acta, v. 186, p. 105–119.

Sillitoe, R.H., and Perelló, J., 2005, Andean copper province: Tectonomagmatic settings, deposit types, metallogeny, exploration, and discovery: Economic Geology, 100th Anniversary Volume, p. 845–890.

Skewes, M.A., and Stern, C.R., 1995, Genesis of the giant late Miocene to Pliocene copper deposits of central Chile in the context of Andean magmatic and tectonic evolution: International Geology Reviews, v. 37, p. 893–909.

Skewes, M.A., Holmgren, C.M., and Stern, C.R., 2003, The Donoso copper-rich, tourmaline-bearing breccia pipe in central Chile: Petrologic, fluid inclusion and stable isotope evidence for an origin from magmatic fluids: Mineralium Deposita, v. 38, p. 2–21.

Slack, J.F., 1996, Tourmaline associations with hydrothermal ore deposits: Reviews in Mineralogy, v. 33, p. 559–643.

Suzuoki, T., and Epstein, S., 1976, Hydrogen isotope fractionation between OH-bearing minerals and water: Geochimica et Cosmochimica Acta, v. 40, p. 1229–1240.

Taylor, H.P., 1979, Oxygen and hydrogen isotope relationships in hydrothermal mineral deposits, in Barnes, H.L., ed., Geochemistry of hydrothermal ore deposits, 2nd ed.: Wiley Interscience, New York, p. 236–277.

Testa, F.J., 2019, Geology, alteration, mineralization and geochemistry of tourmaline breccia complexes in the Andes: Río Blanco-Los Bronces, Chile and San Francisco de los Andes, Argentina: Unpublished PhD dissertation, CODES, University of Tasmania, Australia, 460 p.

Tornos, F., Wiedenbeck, M., and Velasco, F., 2012, The boron isotope geochemistry of tourmaline-rich alteration in the IOCG systems of northern Chile: Implications for a magmatic-hydrothermal origin: Mineralium Deposita, v.47, p. 483– 499.

Toro, J.C., Ortúzar, J., Zamorano, J., Cuadra, P., Hermosilla, J.M., and Spröhnle, C., 2012, Protracted magmatic-hydrothermal history of the Río

Blanco-Los Bronces district, central Chile: Development of world's greatest known concentration of copper: Society of Economic Geologists, Special Publication no. 16, p. 105–126.

Trumbull, R.B., and Slack, J.F., 2018, Boron isotopes in the continental crust: Granites, pegmatites, felsic volcanic rocks, and related ore deposits, *in* Marschall, H.R., and Foster, G.L., eds., Advances in isotope geochemistry: Boron isotopes: The fifth element: Heidelberg, Berlin, Springer-Verlag, p. 249–272.

Vargas, R.A., Gustafson, L.B., Vukasovic, M., and Tidy, E.A., 1999, Ore breccias in the Río Blanco-Los Bronces porphyry copper deposit, Chile: Society of Economic Geologists, Special Publication no. 7, p. 281–298.

Ward, K.M., Delph, J.R., Zandt, G., Beck, S.L., and Ducea, M.N., 2017, Magmatic evolution of a Cordilleran flare-up and its role in creation of silicic crust: Scientific Reports, v. 7, article 9047, doi: 10.1038/s41598-017-09015-5.

Warnaars, F.W., Holmgren, C.M., and Barassi, S.R.L., 1985, Porphyry copper and tourmaline breccias at Los Bronces-Río Blanco, Chile: Economic Geology, v. 80, p. 1544–1565.

Wiedenbeck, M., Trumbull, R.B., Boyce, A., Fournelle, J.F., Franchi, I., Halama, R., Harris, C., Lacey, J.H., Marschall, H., Meixner, A., Pack, A., Rosner, M., Spicuzza, M.J., Valley, J.W., and Wilke, F., 2021, Tourmaline reference materials for the in situ analysis of oxygen and lithium isotope composition: Geostandards and Geoanalytical Research, v. 45, p. 97–119.

Wittenbrink, J., Lehmann, B., Wiedenbeck, M., Wallianos, A., Dietrich, A., and Palacios, C., 2009, Boron isotope composition of melt inclusions from porphyry systems of the Central Andes: A reconnaissance study: Terra Nova, v. 21, p. 111–118.

Wörner, G., Mamani, M., and Blum-Oeste, M., 2018, Magmatism in the central Andes: Elements, v. 14, p. 237–244.

Yáñez, G., Ranero, C.R., von Huene, R., and Diaz, J., 2001, Magnetic anomaly interpretation across a segment of the Southern Central Andes (32–34° S): Implications on the role of the Juan Fernández Ridge in the tectonic evolution of the margin during the upper Tertiary: Journal of Geophysical Research, v. 106, p. 6324–6345.

Yavuz, F., Karakaya, N., Yıldırım, D.K., Karakaya, M.Ç., and Kumral, M., 2014, A Windows program for calculation and classification of tourmaline-supergroup (IMA-2011): Computers & Geosciences, v. 63, p. 70–87.

Zajacz, Z., Halter, W.E., Pettke, T., and Guillong, M., 2008, Determination of fluid/melt partition coefficients by LA-ICPMS analysis of co-existing fluid and silicate melt inclusions: Controls on element partitioning: Geochimica et Cosmochimica Acta, v. 72, p. 2169–2197.

Michael Hohf is an exploration geoscientist with 16 years of academic and field experience associated with the study and understanding of porphyry copper systems. While investigating the world-class Chuquicamata and Río Blanco-Los Bronces districts, he received his undergraduate degree from the Universidad de Concepción (2003) and his Ph.D. degree from the Technische Universität Bergakademie Freiberg (2021). He has worked on exploration projects for several companies including Teck, CODELCO, and BHP, being part of the discovery team of the hypogene copper mineralization of the Chimborazo project in the La Escondida mining district. He is interested in magmatic and hydrothermal processes, their duration, and footprints for effective mineral exploration.